Morphology and symmetry driven by lattice accommodation in polycrystalline bcc-fcc core-shell metallic nanoparticles

Anne Ponchet, Nathalie Tarrat, Teresa Hungria, Magali Benoit, Marie-José Casanove, Patrizio Benzo

Revised manuscript JAP23-AR-02854R (2023)

Morphology and symmetry driven by lattice accommodation in polycrystalline bcc-fcc core-shell metallic nanoparticles

A. Ponchet[1*], N. Tarrat[1], T. Hungria[2], M. Benoit[1], M.-J. Casanove[1], and P. Benzo[1]

[1] CEMES, CNRS, Université de Toulouse, 29 rue Jeanne Marvig, BP94347, 31055 Toulouse Cedex 04, France

[2] Centre de Microcaractérisation CASTAING, Université Toulouse 3 Paul Sabatier, Toulouse INP, INSA Toulouse, CNRS, Université de Toulouse, 3 Rue Caroline Aigle, 31400 Toulouse – France

Abstract

Bcc-fcc multi-metallic nanoparticles associating a single-crystal core (Fe, FeCo alloys…) with a polycrystalline noble metal shell (Au, AuAg alloys …) are perfectly symmetrical or more irregular, even dramatically dissymmetrical, yet presenting a good crystalline organization. Here a combination of experimental analysis and theoretical symmetry analysis is proposed, in order to provide a unified description of the observed morphologies (Fe-Au and Fe-AuAg systems), whatever their symmetry, and predict some morphology variability in a population of nanoparticles. First the central role of the crystal lattice accommodation is comprehensively analyzed from the experimental Fe-AuAg system. The two possible bcc-fcc epitaxial relationships generate a core-shell interface in the shape of a truncated rhombic dodecahedron. This results in two different types of grains in the shell which are elastically accommodated between them by an equal distribution of twins and low angle grain boundaries, however at the cost of internal stresses. At the same time, a symmetry breaking results from two possible growth variants originating from the Nishiyama-Wasserman epitaxial relationships. The shell grains fit together in a nano-puzzle-like organization, resulting in a large number of possible arrangements distributed in 13 different point groups of symmetry, all of lower order than the core symmetry (highest order of cubic symmetry). If the variants are randomly distributed, the probability for the nanoparticle to be asymmetric (group 1) is 80%. The dissymmetrical development of the nanoparticles is then discussed. Extending this approach to other core shapes succeeds in predicting dissymmetrical or dramatically off-centered morphologies experimentally observed in Fe-Au nanoparticles.

*Corresponding author anne.ponchet@cemes.fr

I. Introduction

Nanoparticles (NPs) are extensively studied for their unique properties that combine size and surface effects with intrinsic properties of their components. Multifunctionality or exalted properties may be even promoted in multi-phased NPs [1-4]. For instance, associating Fe based cores with a noble metal as shell offers several potential opportunities: prevent the core from oxidation, protect its magnetic properties, provide a good biocompatibility and propose large surfaces for functionalization (as adsorption of biomolecules…) using less noble metal than monometallic NPs. These properties depend on the NP structure, including its chemical composition, chemical order, morphology and size [1-4]. The origins of NP structures and morphologies are to be found in their mechanisms of formation, i.e. the driving forces at play and the kinetic mechanisms that hinder or favor the pathway towards equilibrium shapes. Multi-phased NPs are also constrained by the accommodation of the different phases, resulting in either the so-called Janus (partial wetting) or core@shell (complete wetting) chemical order. The properties of crystalline NPs are in addition sensitive to atomic arrangements, defects, and nature of surfaces, and the formation of multi-phased crystalline NPs is also driven by the construction of the crystalline interface that accommodates the different lattices.

Symmetry is also one of the characteristics governing the properties of crystalline NPs. Investigating the origin of symmetry breaking in NPs compared to bulk components is receiving much attention [4, 5]. As localized surface plasmon resonances or magneto-plasmonic properties of metallic nanostructures are sensitive to shape, size, surface, strain and defects, symmetry reduction offers new opportunities to tune these properties [6-10]. The symmetric or dissymmetrical configuration of multi-phased NPs (either core@shell, Janus, or containing cavities) can lead to quite different optical responses, depending on the centered or off-centered character of the plasmonic phase (its thickness being then homogenous or not), and on the shape of the plasmonic phase (corners, vertices, size and shape of facets and interfaces…) [6, 8-10]. For catalytic properties of NPs or their functionalization by molecule adsorption, surfaces with a large number of low-coordinated atoms are desirable, which strongly depends on the nature, size and shape of the crystalline facets and edges, all being symmetry-related [6, 11-13]. Symmetry reduction can be due, for instance, to finite size effects modifying the atomic arrangements compared to the bulk crystal, to twins (or other planar defects), to coalescence mechanisms and/or to kinetics effects leading to non-equilibrium morphologies (nanowires for instance) [4, 5]. Regarding multi-phased NPs, the Janus ones are thus, quite obviously, less symmetrical than their bulk components. Comprehensive studies were devoted to symmetry breaking in isostructural core@shell NPs, namely fcc@fcc [14-16], including the notable case of decentering of the core due to a mechanism of internal stress relaxation.

Understanding and even predicting the morphologies of NPs is thus a current challenge that requires a detailed knowledge of all the mechanisms likely to tune not only the size, the chemical order but also the symmetry [4, 5]. A population of NPs is even more complex, due to the distribution of these characteristics over certain ranges [4]. Controlling or predicting their properties requires to investigate individual NPs, but also to gain an insight into the structure variability at the scale of a NP population. Investigating experimentally individual NPs is challenging, due to their small size and to the difficulty to recover the complete three-dimensional (3D) morphology from 2D imaging. Describing a NP population is in addition fragmentary, particularly due to the selection bias (only a few NPs can be analyzed, generally among the most perfect, and they may not be representative of the population). Models describing experimental NPs in a rational way are thus very desirable, particularly when their construction relies on the understanding of the mechanisms of formation, and describes not only single NPs, but also NP populations.

Here we focus on the relationships between lattice accommodation, morphology and symmetry in multi-phased NPs that associate a face-centered cubic (fcc) noble metal, namely Au or Ag and their alloys, with a body-centered cubic (bcc) metal, namely Fe, or with a cubic B2 metal as ordered CoFe and FeRh alloys. Our aim is to provide a unified description of the observed core@shell morphologies, whether they are highly symmetric or highly dissymmetric.

There are two well-known epitaxial relationships between Au (fcc) and Fe (bcc) [17, 18], respectively the Bain one {001}bcc <110>bcc // {001}fcc <100> fcc, and the Nishiyama-Wasserman one {110}bcc <001>bcc // {111}fcc <$1\bar{1}0$>fcc (in the following, the crystallographic indices will be systematically accompanied either by bcc or fcc to distinguish the core and the shell, respectively). Thanks to their large difference in surface energy [19], the growth mode of Au on Fe substrates is 2D Franck-van-der-Merve (full wetting) [20]. As the two metals present a large gap of miscibility [21], using Fe nanocrystals as nano-substrates thus leads to a core@shell chemical order [22, 23]. Once a full wetting layer of 2-3 Au monolayers is formed, a Fe@Au NP is very stable against dewetting. A core@shell chemical order with a full Au wetting layer is also reported with CoFe or FeRh cores [24, 25].

Thanks to the two possible epitaxial relationships, in the general case, the ideal shape of the interface between the core and the shell is a rhombic (or rhombohedral) dodecahedron truncated by {001}bcc faces (Fig.1), improperly referred as truncated rhombic dodecahedron latter on. It consists in 12 hexagonal {110}bcc and 6 square {001}bcc faces, topped by grains of the noble metal growing in the <111>fcc and <001>fcc directions, respectively.

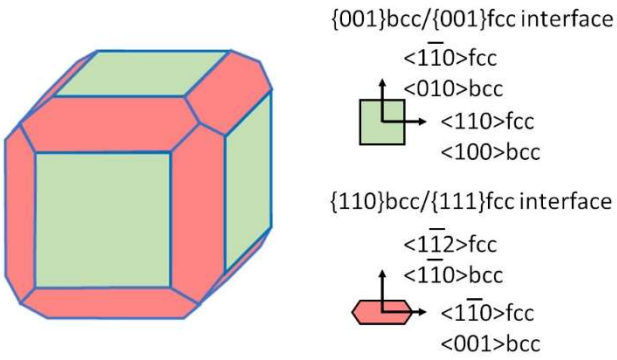

Fig.1. Generic shape of the 3D interface of bcc@fcc NPs, formed by 12 hexagonal {110}bcc and 6 square {001}bcc faces.

In previous works [20, 26], different experimental morphologies of Fe@Au NPs obtained with small Fe cores (5-10 nm) were elucidated as being equilibrium shapes resulting from the competition between surfaces, core@shell interface and grain boundaries. The equilibrium shape evolves with the Au/Fe volume ratio. When the Au amount is just sufficient to form a thin wetting layer, the equilibrium shape of the NPs is close to a truncated rhombic dodecahedron [20]. With a large Au/Fe volume ratio, it consists in a simple Fe cube with 6 square {001}bcc faces topped by Au pyramids growing in <001>fcc directions, because the {001}Fe/{001}Au interface has a much lower energy than the {110}Fe/{111}Au one. At the same time, the pyramidal shape bounded by {111}fcc and top {001}fcc facets (the two most stable surfaces of noble metals [27-29]) contributes to minimize the total NP energy [20].

Beside these rather regular and well-centered morphologies with a quasi-cubic symmetry (Fig.2(a)) reported in Fe@Au [22, 26] and in CoFe@Au NPs [24], morphologies with lower symmetries were also observed. In a recent experiment [30], the Fe@Au NPs formed with a larger core (in the range 10-20 nm) were no longer centered (so called off-centered NPs). The large cores themselves were no longer completely cube-shaped (that can be accounted for by kinetic limitations preventing the interface to reach its equilibrium shape), but the strong dissymmetry of the shells was even more dramatic (Fig.2(b)). None of the causes of symmetry breaking mentioned above could satisfactorily explain these observations. For instance, the stress relaxation mechanism leading to a core decentering, as investigated in the isostructural fcc@fcc systems [14-16], cannot explain here the strong shell dissymmetry, because the elastic energy is negligible compared to the surface and interface energies [22]. The possible role of kinetics mechanism remains also very speculative.

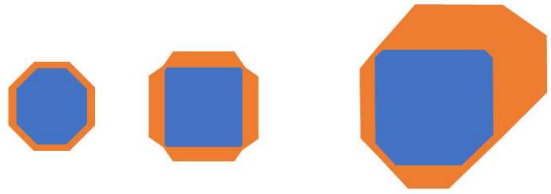

(a) Fe@Au NPs with a cubic symmetry and a centered core

(b) Fe@Au NP with a strongly dissymmetrical shell and an off-centered core

Fig.2. Morphologies of Fe@Au NPs displaying (a) a cubic symmetry with a centered core or (b) an off-centered core and a strongly dissymmetrical shell [20, 22, 26, 30].

The AuAg alloy is another candidate to produce core@shell NPs with Fe. Indeed, Ag and Au crystallize in the same fcc structure without lattice parameter misfit between them and they are miscible. In addition, Ag forms the same epitaxial relationships with Fe as Au does [31] and is expected to fully wet Fe, from density functional theory (DFT) calculation [32]. The equilibrium shape of the interface of Fe@Ag NPs predicted by DFT calculation [32] is a truncated rhombic dodecahedron (not yet observed).

The manuscript is organized as follows: thanks to the growth and structural analysis of Fe@AuAg NPs (section II), we propose a comprehensive description of the various mechanisms accommodating the crystalline lattices in bcc(core)@fcc(shell) NPs, with here a focus on the polycrystalline shell (section III). It allows to demonstrate that there exists a symmetry breaking with a crystallographic origin, intrinsic to bcc@fcc systems (section IV). We then explore systematically the symmetries that a NP can possess with a highly symmetrical core, and discuss how this leads to a dissymmetrical development of the shell (section V). Finally, we extend our approach to irregular and dissymmetrical core shapes and we discuss the origin of highly dissymmetrical morphologies as experimentally observed in large off-centered Fe@Au NPs (section VI).

II. Experimental analysis

Fe@AuAg NPs were grown by dc magnetron sputtering in a Mantis ultra-high vacuum (UHV) chamber using high purity Fe, Ag and Au elemental targets and an amorphous silica substrate itself deposited on NaCl crystals. The Fe and AuAg layers were sequentially deposited at a same temperature of 600°C with a growth rate of 0.007 nm/s and 0.014 nm/s, respectively. The nominal deposited thicknesses were 1.6 nm, 0.6 nm and 0.6 nm for Fe, Au and Ag respectively. Once formed

the NPs are protected by a 5 nm thick amorphous silica cover layer deposited at room temperature. This procedure is the same as the one described for Fe@Au NPs in [26, 30].

A plan-view specimen was prepared for atomically resolved high-angle annular-dark field (HAADF) scanning transmission electron microscopy (STEM) experiments using a JEOL ARM200F cold FEG probe-corrected microscope, by transferring the SiO_2 films containing the metallic layers onto TEM copper grids, after dissolution of the NaCl substrate in deionized water.

Fig.3(a) displays a Fe@AuAg NP observed in plan-view by HAADF-STEM, that at first glance is relatively regular in shape. First of all, the core@shell chemical order is clearly highlighted both by the different intensities of the core and the shell, and by the two different crystalline lattices. A complete crystallographic analysis of the NP is displayed in Fig.3(b).

The core forms a single bcc crystal, here observed along a <001>bcc direction. The observed 2D section of the core is close to an octagon, with four large edges along the <100>bcc directions, and four smaller edges along the <110>bcc directions. This well corresponds to a 2D section in a {001}bcc plane from a truncated rhombic dodecahedron (Fig.1).

The shell exhibits the typical atomic arrangements of fcc crystals seen perpendicularly to a <110>fcc direction. Two different interface types are identified:

(i) {001}bcc/{001}fcc interfaces (green lines) are abrupt and straight. They generate a coherent, quasi perfect epitaxial growth of the shell.

(ii) {110}bcc/{111}fcc interfaces (red lines) are abrupt but not straight: they form small steps with a regular pattern, with a periodicity of 5 bcc atoms (Fe) and 4 fcc atoms (Au or Ag) along the <110>bcc//<112>fcc directions.

Consistently with the existence of two interface types, we identify two growth orientations and as many grains in the shell as the core has faces visible in Fig.3(b), i.e. four grains growing in a <001>fcc direction (from a {001}bcc/{001}fcc interface) and four grains growing in a <111>fcc direction (from a {110}bcc/{111}fcc interface), hereafter named <001>fcc and <111>fcc oriented grains, respectively. In Fig.3(b), in each grain, one or two elementary 2D cells are inserted for identifying the fcc grain orientation.

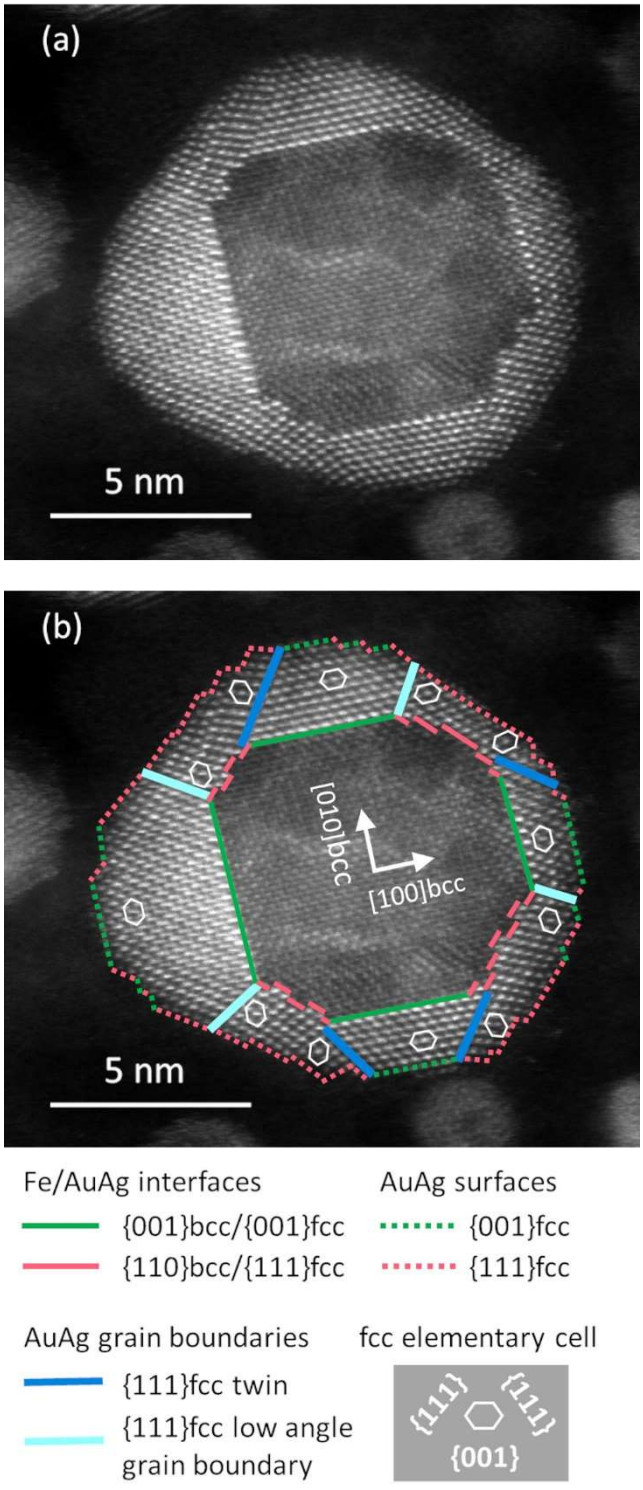

Fig.3 (a) Atomically resolved HAADF-STEM image of a Fe@AuAg NP, observed along a <001>bcc direction. (b) Structural analysis of the NP.

Adjacent <111>fcc and <001>fcc oriented grains share a {111}fcc plane, forming the grain boundary. These grains boundaries can be classified into two types depending on the relative disorientation between the two grains:

(i) There is a change in the atomic stacking on either side of the grain boundary, which is therefore a {111}fcc twin (in dark blue in Fig.3). The two adjacent grains then display a large disorientation.

(ii) There is no change in the atomic stacking at the boundary (in light blue), but the two adjacent grains are slightly disoriented. These boundaries will be referred to as low angle grain boundaries (LAGB). Considering that there are two different adjacent grains or one single distorted grain is questionable. However, within the framework of epitaxial growth, it is relevant to define two different grains from the observed interfacial relationships.

Each grain is well crystallized and free of extended defects originating from the interfaces. No dislocation is observed along the boundaries. One dislocation is nevertheless seen inside the top left <111>fcc oriented grain.

Finally, green and red dotted lines are used as eye guides respectively for the traces of the {001}fcc and {111}fcc planes forming the NP surface.

III. Coherent and incoherent accommodation of the different crystallites

The accommodation of the crystalline lattices due to this polycrystalline NP geometry is complex and involves the combination of several mechanisms. The accommodation of fcc and bcc lattices at the core@shell interface was already analyzed in previous works [22, 26] and is similar to that reported for the Au/Fe [18] and Ag/Fe [31] 2D heteroepitaxy:

(i) The perfect {001}bcc/{001}fcc interface is due to the well-known Bain epitaxial relationship [17]. It is fully coherent thanks to the small effective 0.6% misfit existing in the two <001>bcc//<110>fcc directions of the interfacial plane (the misfit is similar for Au/Fe and Ag/Fe).

(ii) The {110}bcc/{111}fcc interface is attributed to the Nishiyama-Wasserman (NW) epitaxial relationship [17], that remains coherent in the <001>bcc//<110>fcc direction (0.6% misfit) but is expected to be incoherent in the <110>bcc//<112>fcc direction (23% misfit).

The NP observed here allows to provide a more accurate and comprehensive description of the lattice accommodation than already reported. It first provides a very direct evidence of the NW

interfacial arrangement at the nanometric scale of a NP. The step patterns observed at the {110}bcc/{111}fcc interfaces in Fig.3 have exactly the periodicity expected for the coincidence network recovering the 23% misfit, i.e. 4 fcc for 5 bcc atoms. This coincidence network corresponds to the introduction of a misfit dislocation every 4 fcc or 5 bcc atomic columns. The steps probably reduce the local distortion due to the dislocation network.

(See Supplementary Material for more details on the misfit accommodation and dislocations at bcc-fcc interfaces).

This NP also gives new insights on the accommodation mechanisms due to the polycrystalline character of the shell. As pointed out in section II, the lattices are fully coherent throughout the whole shell, without dislocations. An elastic distortion of the lattice is directly visible in each <111>fcc oriented grain: elemental 2D cells taken at two different places of a grain are significantly disoriented (Fig.3(b)). To quantify this distortion, we report in Fig.4(a) the angles between the two boundaries of each grain (measured from Fig.3(b)) and compare them with the angle between two {111}fcc planes in the relaxed fcc crystal, i.e. 0° or 70.53° (or its complement 109.47°). In the four <001>fcc oriented grains, the angles between the two {111}fcc boundaries are -3°, -7°, -70° and 63° respectively (with an error bar in the measurements of +/- 2°). The average shift from the relaxed bulk situation (0°, 0°, -70.53° and 70.53°) is -4.2° with a standard deviation (SD) of 3.2 °. In the four <111>fcc oriented grains, the measured angles between the two {111}fcc boundaries are 92°, 95°, 97° and 93°, respectively (error bar +/-2°). The average value is 94.2° with a SD of 1.9° and the average shift from the relaxed bulk situation (109.47°) is thus -15.3° with a SD of 1.9°.

This reveals internal stresses. A part of these stresses originates from the residual misfits at the bcc-fcc interfaces. They are however rather small, and the modification of the angle that they induce between two families of {111}fcc planes (around 1°, see Supplementary Material for more details) is negligible compared to the measured shifts.

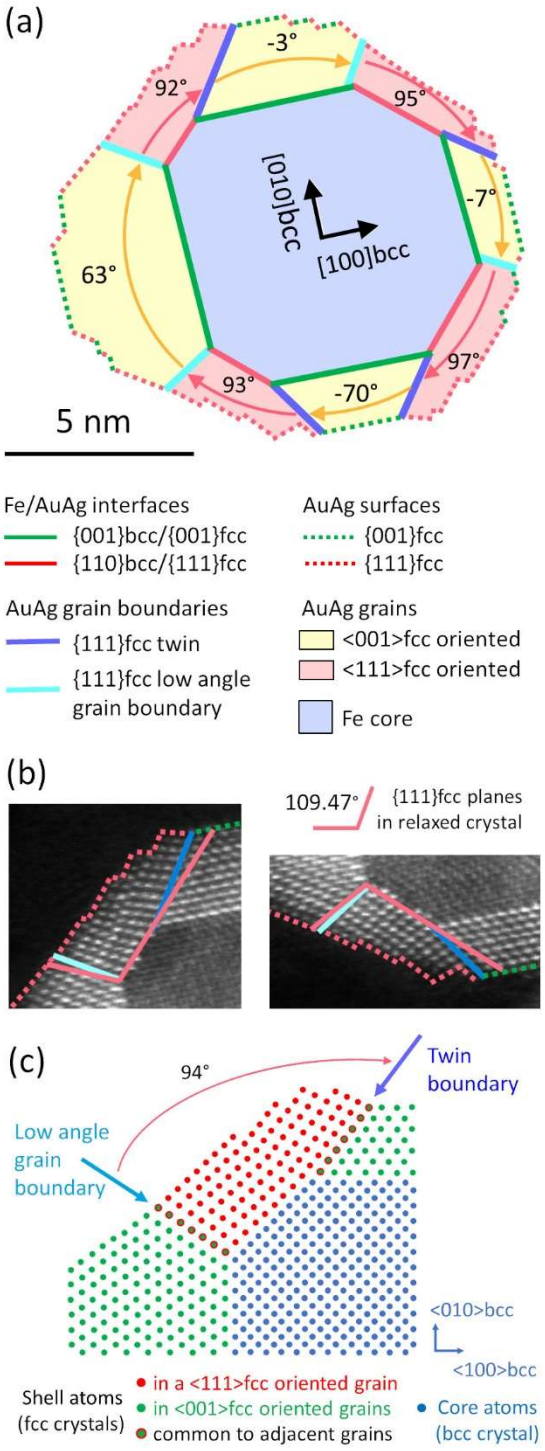

Fig.4 (a) Angles between the grain boundaries, measured from Fig.3(b). (b) Zoom on two <111>fcc oriented grains. One red line prolongates the interface and forms a 109.47° angle with the other one, as expected between two {111}fcc planes in a relaxed crystal. The blue lines show the actual location of the {111}fcc planes forming the boundaries. Note the presence of one dislocation inside the left grain. (c) Schematic representation of the atomic arrangement in <001>bcc 2D section (only a quadrant is shown), with the average experimental angle (94°) between the LAGB and the twin. (In this scheme, the size of the {110}bcc//{111}fcc interface corresponds to one complete period of the

coincidence network (see Supplementary Material for more details). An incomplete coincidence network would result in a small additional misfit at the interface and eventually a shift by one plane of the twin.)

To identify the major contribution to these large shifts, one has to compare a relaxed crystal with the grains as they actually coexist in the shell (Fig.3(b)). As the angle between two different {111}fcc planes in the relaxed fcc crystal is 0°, 109.47° or its complement 70.53°, associating the four <111>fcc oriented grains with the four <001>fcc oriented grains in relaxed state to form a shell, while being bounded by shared {111}fcc planes, would require (starting from the top left grain, in the clockwise direction):

$$109.47° + 0° + 109.47° + 0° + 109.47° - 70.53° + 109.47° + 70.53° = 437.88°$$

Since there are only 360° available, there is an angular gap of -77.88°. (Note that the contributions from the <001>fcc grains cancel each other out). This angular gap is distributed as -19.47° per quadrant consisting in one <111>fcc oriented grain and two half <001>fcc oriented grains, or as -9.74° per boundary (see Appendix A for more details). Consequently, the eight grains can coexist only at the cost of some internal stress. This stress originating from the boundaries is essentially compressive, biaxial in the {001}fcc planes parallel to the interfaces for the <001>fcc oriented grains, and uniaxial in the <112>fcc interfacial direction for the <111>fcc oriented grains (with probably shear components).

The two average shifts, -4.2° (SD 3.2°) and -15.3° (SD 1.9°), express how the theoretical angular gap (-19.47° per quadrant) is experimentally distributed in the two types of grains. So, the stress induced by the geometrical accommodation in the shell is shared by all the grains, but it is significantly larger in the <111>fcc than in the <001>fcc oriented ones (Fig.4(b) and (c)). The curvature of the atomic planes is visible inside each of the four <111>fcc oriented grains; the {111}fcc planes parallel to the interface are especially curved at the vicinity of the point of intersection between the {110}bcc//{111}fcc interface, the {001}bcc//{001}fcc interface and the twin boundary (Fig.3(a) and 4(b)). This is schematically depicted in Fig.4(c).

It is worth noticing that grains could have been plastically accommodated with dislocations at the grain boundaries, as usually observed in larger polycrystals. With the disorientation of -9.74° at each boundary, the required distance between dislocations (one every 6 atomic planes, approximatively) is however of the same order of magnitude as the shell thickness (for more details,

see Appendix A). This is then not surprising to observe elastic accommodation and no dislocations. In addition, similarly to the Stranski-Krastanov growth mode in highly mismatched systems [33-41], elastic rather than plastic relaxation is favored by the numerous free surfaces of the grains, that partially release the stress (especially via steps at the surface of the <111>fcc oriented grains). Some transfer of stress into the core can also contribute to reduce the total elastic energy [22, 37, 41]. The isolated dislocation inside one <111>fcc oriented grain (Fig.4(b)) can also be understood as reducing the internal compressive stress.

Finally, the accommodation of the lattices at the junction between three adjacent <111>fcc oriented grains is not experimentally accessible, and is possibly source of additional defects, stresses and local distortions.

To summarize, in this NP there are different mechanisms of lattice accommodation and stress relaxation:

(i) The bcc and fcc crystals are coherently accommodated along the <001>bcc//<110>fcc directions, that generates a small compressive stress, biaxial in the <001>fcc oriented grains and uniaxial in the <111>fcc oriented grains.

(ii) The bcc and fcc crystals are incoherently accommodated along the <110>bcc//<112>fcc directions with an interfacial coincidence network of 5 bcc versus 4 fcc atoms (concerns <111>fcc oriented grains).

(iii) The accommodation between <111>fcc and <001>fcc oriented grains of the shell is fully coherent, thanks to boundaries formed by {111}fcc planes shared by the two grains. No dislocation is visible along the grain boundaries.

(iv) This coherent accommodation between <111>fcc and <001>fcc oriented grains is unavoidably accompanied by an elastic lattice distortion in the shell, generating a stress mainly compressive in the <111>fcc and <001>fcc oriented grains. This is due to an angular gap of -19.47° over 90° per quadrant.

(v) A dislocation inside a <111>fcc oriented grain can contribute to relax the internal stress in the shell.

(vi) Partial stress relaxation can occur through free surfaces.

(vii) Some stress can be transferred to the core.

The points (i) and (ii) result from the lattice misfits between core and shell, while (iii) to (v) are due to the geometrical constraints to build the polycrystalline shell.

IV. From lattice accommodation to symmetry breaking in bcc@fcc NPs

In this section, the case of the studied NP is used to explore the links between the lattice accommodation and the NP morphology, and a generalization of these links is introduced. Fig.3 brings indeed to light some dissymmetry in the shell morphology: (i) The grains boundaries are not distributed symmetrically. (ii) The four <001>fcc oriented grains do not display the same morphology. (iii) On the contrary, all <111>fcc oriented grains display a relatively similar morphology.

The shell dissymmetry does not find its origin in the core shape, the visible 2D section of the core being assimilable to the cross-section of a truncated rhombic dodecahedron. The non-symmetrical distribution of the boundaries allows to identify a crystallographic origin. The symmetry breaking is a consequence of the epitaxial growth. While for a <001>fcc oriented grain, the plane normal to the interface and to the section plane is a symmetry element (it is indeed a {110}fcc plane), it is not the case for a <111>fcc oriented grain: As a consequence, two crystallographic variants of a <111>fcc oriented grain can grow on a {110}bcc core face, depending on the stacking of the {111}fcc planes parallel to the interface.

The symmetry loss resulting from all the possible distributions of four variants in a plane is reviewed in Fig.5. The octagonal cross-section of a bare core has a high order of symmetry with a 4-fold axis and four mirrors (Fig.5(a)). Then the variants are symbolized by arrows oriented either in the clockwise or counter-clockwise direction, depending on the direction of the {111}fcc planes stacking. The variant distribution displayed in Fig.5(b) has a 4-fold axis symmetry but no mirror; in Fig.5(c) it has a 2-fold axis symmetry and two mirrors; in Fig.5(d) it has one mirror; in Fig.5(e) it has no symmetry. These symmetries apply only for a distribution of four variants in a plane but do not presume the 3D symmetry. (Note also that the angular gap is

$$360° - 4x109.47° = -77.88°$$

in all cases, the contributions of the <001>fcc oriented grains cancelling each other out as in the experimental case).

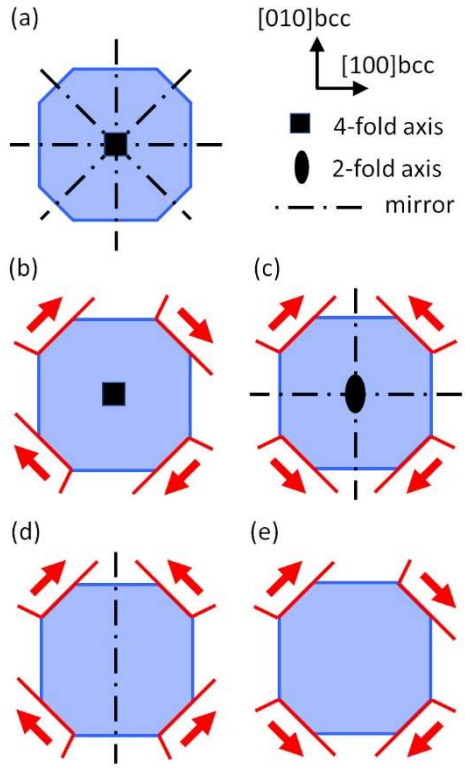

Fig.5. Symmetry reduction due to four variants in a plane (analysed in 2D section). (a) Initial symmetry of a {001}bcc cross-section of the core. (b)-(e) For each {110}bcc face, the red lines indicate the two families of {111}fcc planes of the <111>fcc oriented grain likely to grow on it. The arrows symbolize the variants. The four different possible configurations are displayed from the highest order of symmetry (b,c) to the complete loss of symmetry (e); (e) corresponds to the experimental 2D section displayed in Fig.3.

As a result, one <111>fcc oriented grain is necessarily separated from one of its two <001>fcc oriented neighbors by a LAGB and from the other one by a twin. Reversely, one <001>fcc oriented grain can be separated from its two neighbors visible in 2D section by two LAGB, two twins, or one LAGB and one twin. These three different possible configurations exist in the observed NP (Fig.3(b)). The morphologies of the <001>fcc oriented grains are then fully determined by the distribution of the <111>fcc oriented variants.

To summarize, there is a loss of the symmetry with a crystallographic origin: the existence of two possible variants for the <111>fcc oriented grains. It has no impact on the morphology of the <111>fcc oriented grains themselves, but it dramatically impacts the morphology of the <001>fcc oriented grains.

In the next section, the impact of the variant distribution on NP symmetry and morphology will be considered in 3D.

V. NP symmetry and 3D shell morphology with a truncated rhombic dodecahedron core

In this section, we intend to explore in 3D the possible NP morphologies within the constraints imposed by the lattice accommodation i.e. by the fact that each <111>fcc oriented grain is separated from its two neighboring <001>fcc oriented grains by a twin and a LAGB, respectively. To decorrelate the respective roles of the core shape and of the lattice accommodation, here the core is modeled by 6 identical {001}bcc and 12 identical {110}bcc faces.

In the following, symmetry breaking will be used relatively to the core symmetry.

A. 3D representation of the symmetry breaking and of the resulting NP morphology

Understanding the NP morphology requires to consider now the lattice accommodation in the 3D space. For this purpose, we use a pattern to represent a truncated rhombic dodecahedron (Fig.6(a-c)). The pattern in Fig.6(a) symbolizes the 3D interface (or bcc core) shape: the square and hexagonal faces correspond to the two interface types, respectively generating the six <001>fcc and twelve <111>fcc oriented grains on {001}bcc and {110}bcc faces.

Then we need to represent the symmetry breaking induced by the variants of the <111>fcc oriented grains growing on the {110}bcc faces: the resulting variant distribution will be symbolized by arrows crossing the hexagonal faces in the $<1\bar{1}0>$bcc//$<11\bar{2}>$fcc directions (with the same convention as in Fig.5, i.e. the arrow points toward the {111}fcc planes of the interface).

The consequence of the lattice accommodation is that the morphology of each <001>fcc oriented grain depends on its boundaries, which are four in number in the 3D space. To make it visible, for each <001>fcc oriented grain, a color is attributed to each quarter of its square base, depending on the nearest neighboring variant: Dark or light yellow when the <001>fcc and <111>fcc oriented grains will be separated by a LAGB boundary or a twin, respectively. There are six different possible morphologies of the <001> oriented grains, depending on their four <111>fcc oriented neighbors (Fig.6(d)).

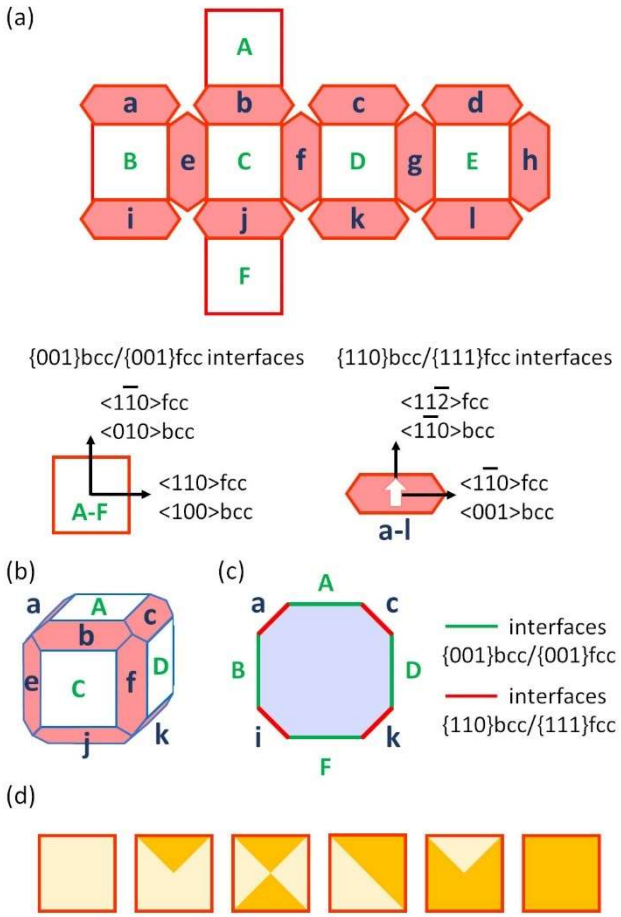

Fig.6 (a) Pattern of a truncated rhombic dodecahedron where the squares and hexagons represent the {001}bcc/{001}fcc and {110}bcc/{111}fcc interfaces, respectively. The white arrow symbolizes the variant of the <111>fcc oriented grain. The letters indicate the correspondence between (a) the pattern and (b) a 3D representation or (c) a 2D section (by the center) in one {001}bcc plane, here parallel to the C and E faces. (d) Schematic representation of the six possible morphologies of a <001>fcc oriented grain growing from a {001}bcc/{001}fcc interface: dark/light yellow shade indicates that the nearest boundary with a <111>fcc oriented grain is a LAGB/twin, respectively.

B. Symmetry as a tool to understand, predict and classify the NPs morphology

Exploring the possible morphologies is like doing a nano-puzzle where six <001>fcc oriented grains, chosen amongst the six possible morphologies of Fig.6(d), have to fit with twelve <111>fcc oriented grains having the same morphology imposed by the lattice accommodation, namely all are bounded to the <001>fcc oriented grains by a LAGB and a twin. Reasoning by symmetry will be used here as a tool allowing to identify and classify all possible solutions of this puzzle.

Some hypotheses are made: (i) The NP is free, i.e. its interaction with the oxide substrate used in the growth process is not considered here. This is experimentally justified as the adhesion of the NP on the substrate is particularly weak and does not inhibit the shell development at the interface between the NP and the oxide substrate [30]. (ii) We can reasonably assume that the boundaries joining three adjacent <111>fcc oriented grains (not experimentally accessible) do not modify the symmetry.

Analyzing the symmetry of a NP consists in determining its point group of symmetry. In the following we use the Hermann-Mauguin notation considering the crystallographic directions of the bcc core as reference (for instance group *3* means that the symmetry elements of the NP are the identity element and a 3-fold axis built from one <111>bcc direction of the core).

The symmetry of the NP as a whole must cover both crystallographic, morphological and orientation symmetries, considering the core, the <111>fcc oriented grains and the <001>fcc oriented ones. Since it is generated by the distribution of the twelve <111>fcc oriented grain variants, it will be entirely symbolized in the patterns by the arrow symmetry.

C. What are the possible symmetries for a NP with a truncated rhombic dodecahedron core?

The symmetry group of a NP is obviously a sub-group of $m\bar{3}m$, the group of the core itself considering both its crystallography and its shape (highest order of cubic symmetry). All the sub-groups of $m\bar{3}m$ are displayed in Fig.7, the relationships between sub- and super-groups being indicated by lines [42] (by definition, all symmetry operators of a sub-group are also contained in its super-groups). However, certain groups are prohibited. Indeed, the symmetry breaking induced by the variants growing on the {110}bcc faces is incompatible with any symmetry involving a {110}bcc plane as a mirror or a <110>bcc direction as a 2-fold axis. This eliminates as possible solutions: $m\bar{3}m$, $\bar{4}3m$ and *432* (cubic symmetry), *4mm*, $\bar{4}2m$, *4/mmm* and *422* (tetragonal symmetry), *3m*, $\bar{3}m$ and *32* (rhombohedral symmetry), all in red in Fig.7

It comes that the groups that can exist for bcc@fcc NPs (in blue) are $m\bar{3}$ (cubic symmetry), *4/m* (tetragonal symmetry), and all their sub-groups. (There are however no NP of sub-groups *23* and *222*, because all NPs with three 2-fold axes have also three mirrors and therefore belong to the $m\bar{3}$ or *mmm* groups. Indeed, the variant pattern, symbolized by the arrow, is located in a {001}bcc plane, so its image by a 2-fold axis parallel to this plane is similar to the image that would be given by a mirror perpendicular to this plane and containing the 2-fold axis.)

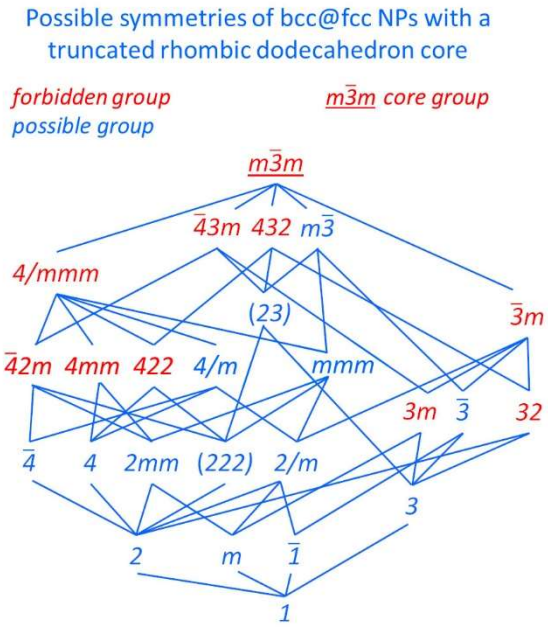

Fig.7: Sub-groups of the *m3̄m* symmetry group. The lines indicate the super-groups/sub-groups relationships, from the highest order of symmetry (top) to the lowest (bottom) [42]. The groups in red cannot exist for bcc@fcc NPs with the truncated rhombic dodecahedron core, because the <111>fcc oriented variants growing on each {110}bcc face are incompatible with any symmetry element involving a {110}bcc plane or a <110>bcc direction. The groups that can exist (in blue) are *m3̄* , *4/m* and all their sub-groups (there are however no NP in groups in parenthesis). The Hermann-Mauguin notation refers to the crystallographic directions of the bcc core.

Fig.8 displays some patterns of high symmetry: (a) The unique cubic pattern, *m3̄* (the 3-fold axes are built from the <111>bcc directions and the mirrors from the {001}bcc planes). (b) The unique *3̄* pattern (rhombohedral symmetry with centro-symmetry and one 3-fold axis). (c) One of the two *4/m* patterns (tetragonal symmetry; the mirror is perpendicular to a 4-fold axis built from one <001>bcc direction). Such patterns fully symbolize the NP morphology generated by the lattice accommodation. To symbolize the <111>fcc oriented grains that are symmetrical between them, their hexagonal bases are represented with the same color. The light and dark yellow shades symbolize the morphology of the <001>fcc oriented grains as defined in Fig.6(d) (the resulting 2D sections of NPs will be discussed later on, in section V.E.).

All the possible solutions are given in Supplementary Material.

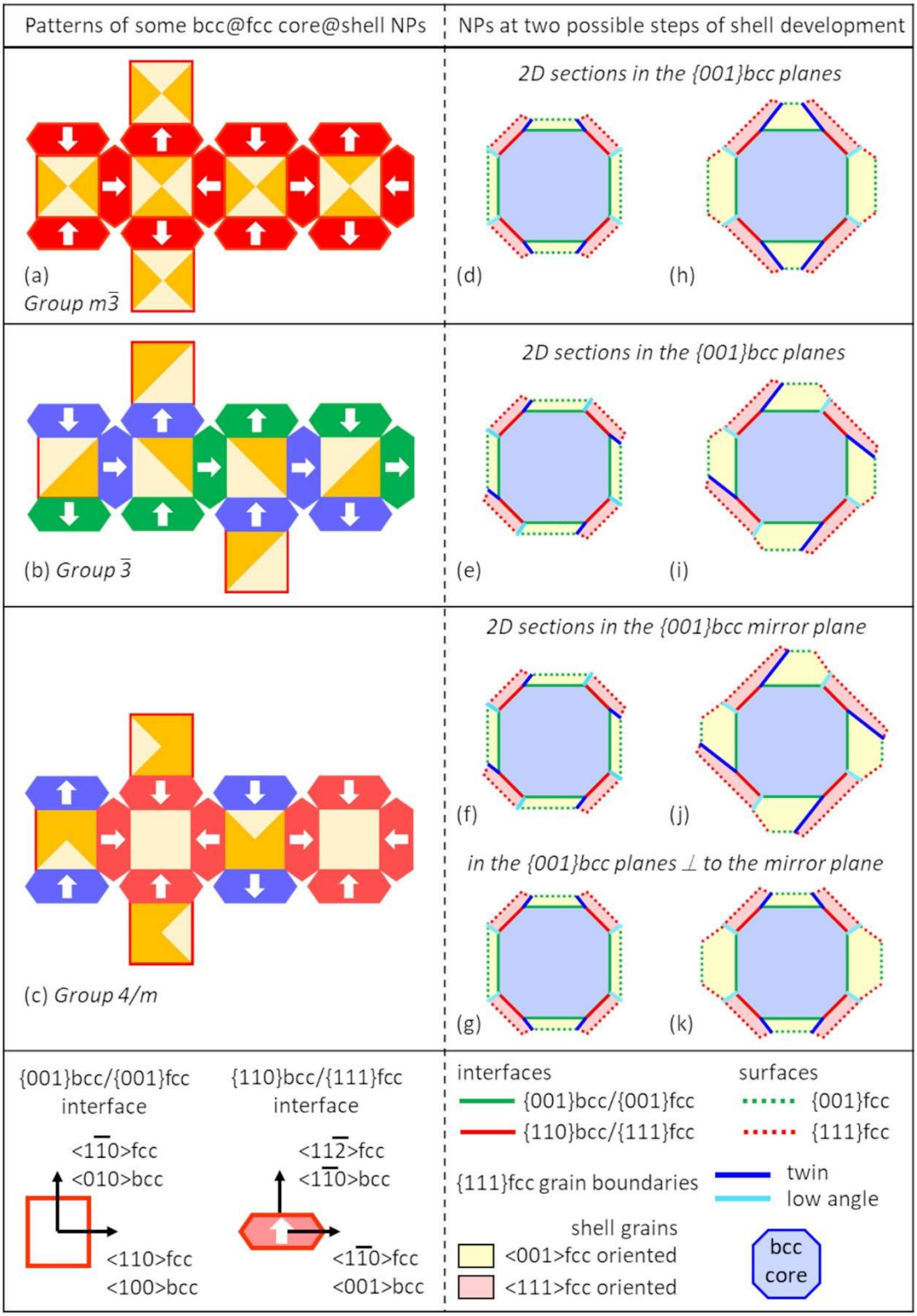

Fig.8 Patterns of some possible bcc@fcc core@shell NP morphologies of high symmetry: (a) only possible *m3̄* pattern; (b) only possible 3̄ pattern; (c) one of the two possible *4/m* patterns. The white arrows symbolize the variant distribution that determines the NP symmetry. The same color for the hexagonal basis of <111>fcc oriented grains means that they are symmetrical to each other. The light and dark yellow shades symbolize the morphology of the <001>fcc oriented grains as defined in

Fig.6(d). For each pattern, two possible steps of shell development are proposed, respecting the symmetry (d-k).

D. Distribution of all possible NP morphologies and symmetries with a truncated rhombic dodecahedron core

Thanks to the symmetry analysis, all different possible NP morphologies can now be predicted and their distribution calculated as a function of the symmetry (Table I). Given the 12 {110}bcc faces, there are 2^{12} possible combinations of the variants, but a much smaller number of morphologies, several combinations being similar in morphology. The number n(*G*) of combinations belonging to a given symmetry group *G* is calculated from a symmetry analysis (detailed in Appendix B) as well as q(*G*) the number of combinations providing the same NP morphology. Then the number of different morphologies p(*G*) is deduced from n(*G*) = q(*G*) x p(*G*). It comes that the 2^{12} combinations can be classified in 186 different possible morphologies distributed in 13 symmetry groups (Table I). The different morphology patterns are displayed in Supplementary Material.

	G		n(*G*)		q(*G*)	p(*G*)
cubic	$m\bar{3}$	(T_h)	2^1	2	2	1
rhombohedral	$\bar{3}$	(S_6)	$4\left(2^2 - \mathrm{n}(m\bar{3})\right)$	8	8	1
	3	(C_3)	$4\left(2^4 - \mathrm{n}(m\bar{3})\right) - \mathrm{n}(\bar{3})$	48	8	6
tetragonal	*4/m*	(C_{4h})	3×2^2	12	6	2
	$\bar{4}$	(S_4)	$3 \times 2^3 - \mathrm{n}(4/m)$	12	12	1
	4	(C_4)	$3 \times 2^3 - \mathrm{n}(4/m)$	12	6	2
orthorhombic	*mmm*	(D_{2h})	$3\left(2^2 - \mathrm{n}(m\bar{3})\right)$	6	6	1
	mm2	(C_{2v})	$3\left(2^5 - \mathrm{n}(mmm) - \mathrm{n}(m\bar{3})\right)$	72	12	6
monoclinic	*2/m*	(C_{2h})	$3\left(2^4 - \mathrm{n}(mmm) - \mathrm{n}(m\bar{3})\right) - \mathrm{n}(4/m)$	12	12	1
	2	(C_2)	$3\left(2^6 - \mathrm{n}(mmm) - \mathrm{n}(m\bar{3})\right) - \mathrm{n}(mm2) - \mathrm{n}(4/m) - \mathrm{n}(2/m) - \mathrm{n}(4) - \mathrm{n}(\bar{4})$	48	12	4
	m	(C_s)	$3\left(2^8 - \mathrm{n}(mmm) - \mathrm{n}(m\bar{3})\right) - 2 \times \mathrm{n}(mm2) - \mathrm{n}(4/m) - \mathrm{n}(2/m)$	576	24	24
triclinic	$\bar{1}$	(C_i)	$2^6 - \mathrm{n}(mmm) - \mathrm{n}(m\bar{3}) - \mathrm{n}(4/m) - \mathrm{n}(2/m) - \mathrm{n}(\bar{3})$	24	24	1
	1	(C_1)	$2^{12} - \sum_{all\ other\ groups} \mathrm{n}(G)$	3264	24	136
total			2^{12}	4096		186

Table I: Distribution of the 2^{12} possible combinations of variants as a function of the NP symmetry group *G*. For each possible group *G*, there exist n(*G*) combinations distributed in p(*G*) different NP morphologies, each morphology being represented by q(*G*) combinations. The Hermann-Mauguin

notation of symmetry groups refers to the crystallographic directions of the bcc core (Schoenflies notation in parenthesis). The systems (cubic, rhombohedral…) do not refer to the crystals, but are used here to characterize the NP symmetry.

The probability for a NP to belong to a particular symmetry group is thus n(*G*)/2^{12} with the hypothesis that the variants are randomly distributed, and the probability to have a particular morphology is q(*G*)/2^{12}. The probability to keep a high order of symmetry by pure chance is thus extremely reduced (for instance it is 2^{-11} for the cubic $m\bar{3}$ and $3x2^{-10}$ for the tetragonal *4/m*, i.e. 0.05% and 0.3%, respectively). About 80% of the combinations are asymmetrical i.e. they do not even have any symmetry except the identity (group *1*).

Symmetry breaking in growth is rarely a purely random process but is initiated by very local mechanisms, that propagate [5]. Here these mechanisms cannot not be recovered experimentally because the interfaces are built (and can even be modified) at the same time as the shell is formed [26]. Nevertheless, the independent nucleation of each <111>fcc oriented grain, as it would be required for a pure random process, is very unlikely. As illustration, we can propose this possible sketch: As the wetting layer (2-3 monolayers) forms, the interface begins to organize from one particular core face and this organization propagates from it, which in itself constitutes a first event of symmetry breaking. For instance let us assume the formation of a first {001}bcc/{001}fcc interface prior to {110}bcc/{111}fcc ones, due to a stronger wetting (from DFT data [20, 32]). This first formed interface could propagate the symmetry breaking in a non-random sequence as shown in Fig.9, where the five first formed grains, being separated by LAGBs, have almost the same orientation.

Many other pathways could select particular morphologies [4], either driven by kinetics or thermodynamics (the issue of the relative stability of the different morphologies being not treated here). In any case, as it is currently out of our reach to control the nucleation at the atomic scale, the Table I suggests that there will be a broad distribution of morphologies and symmetries in a population of NPs.

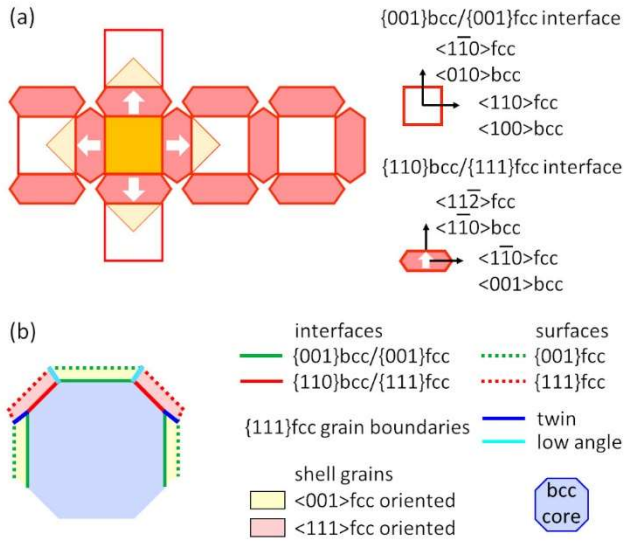

Fig.9 Possible non-random sequence from a first formed {001}fcc/{001}bcc interface: (a) Partial pattern. The white arrows symbolize the variants of <111>fcc oriented grains growing on {110}bcc faces. The light and dark yellow shades symbolize the morphology of the <001>fcc oriented grains as defined in Fig.6(d). (b) NP in 2D section.

E. How the shell dissymmetry is generated and amplified

First, it is worth noticing that, due to the position of the grain boundaries, the shape of the shell grains constantly evolves with increasing the shell volume, whatever the NP symmetry. As we now dispose from the 3D arrangements of the grains, thanks to the symmetry analysis above, we can also understand the more or less dissymmetrical development of the shell.

1. Differential evolution of the grains

In Fig.8(d-k) two different possible steps of the shell development are proposed (seen in 2D section). In the first one, the shell thickness is uniform. This corresponds to the formation of the wetting layer of a few monolayers, as experimentally observed [23, 26] and theoretically predicted from DFT calculation of the wetting factors [20, 32].

In the second step, we propose a differential development of the <001>fcc oriented grains depending on their morphology. Once the interface is covered by several atomic layers of shell, the variant distribution is considered as frozen, due to the very huge energy barrier to be crossed to reverse a variant. However, in our growth conditions close to equilibrium [20, 22, 30], the easy surface diffusion of Au and Ag atoms allows the rearrangement of the shell surface to minimize the

excess energy coming from surfaces. We then do not treat here of a possible differential growth rate during the growth. Rather we focus on the intrinsic impact of the symmetry on the resulting development of the shell with the increase of its volume, prior to any other mechanism. There is no intrinsic reason that two grains with the same morphology evolve differently. Conversely, two grains with different morphologies (as defined in Fig.6(d)) cannot have the same evolution. At the scale of the whole NP, different types of <001>fcc oriented grains thus lead to a dissymmetrical distribution of the shell volume within the grains.

As seen in Fig.4(c), the <001>fcc oriented grain development is locked in each direction where the grain is bounded by a twin. Contrarily, a grain can develop laterally in each direction where it is bounded by a LAGB, and then it forms a free {111}fcc facet. As a result, the lateral development is possible in exactly as many directions as there are LAGBs bounding the grain. The grains bounded by four LAGBs can be topped by well-formed pyramids, keeping a balance between the top {001}fcc and the four lateral {111}fcc facets that contributes to reduce the surface energy [20]. The grains bounded by four twins are locked in all lateral directions; they can develop only in the <001>fcc direction, and the progressive reduction of the {001}fcc top facet could result in the grain being covered by its four <111>fcc oriented neighbors. Experimentally this is not observed, suggesting that these grains stop their growth development before, probably to preserve the balance between {001}fcc and {111}fcc facets. Between these two extremes, other grains have intermediate and dissymmetrical developments.

The different yellow shades in the patterns can thus be used as a guideline for comparing their possible development. The rules chosen to build the shell are:

(i) The shell is terminated by {111}fcc and {001}fcc facets, the most stable in noble metals [27-29], as experimentally observed. Protrusions are avoided.

(ii) The shell is built keeping the symmetry of the variant distribution.

(iii) All <001>fcc oriented grains with the same morphology (as defined in Fig.6(d)) have the same development.

(iv) We chose to differentiate the evolution of the different <001>fcc oriented grains by assigning them different thicknesses, increasing with the number of LAGB boundaries limiting them (0 to 4, from Fig.6(d)).

2. Consequence on the shell dissymmetry

At the first stage, there is an orientational dissymmetry for the <111>fcc oriented grains, which are similar in size and morphology and differ only by their relative orientation, and a morphological dissymmetry for the <001>fcc oriented grains.

At the second stage, the dissymmetry expresses in addition by different thicknesses of the different types of <001>fcc oriented grains (dissymmetry in shell extension). By a retroaction like process, this can induce a differentiation in the development of the <111>fcc oriented grains themselves (dissymmetry in their extension). The amplitude of the shell dissymmetry is thus amplified as the volume shell increases, without change in the symmetry group.

Let us illustrate this dissymmetry amplification, with the different cases in Fig.8:

(a) With the cubic pattern: the shell does not, of course, develop dissymmetry, neither at the first (Fig.8(d)) nor at the second stage (Fig.8(h)).

(b) With the pattern of group $\bar{3}$: being all in symmetrical position between them, the <001>fcc oriented grains remain similar, at each step (Fig.8(e) and 8(i)). The symmetry reduction concerns the orientation of the <111>fcc oriented grains and not the morphology of the <001>fcc oriented grains.

(c) With the pattern of group *4/m*: The morphological dissymmetry affecting the two kinds of <001>fcc oriented grains is visible from the first step (by comparing the sections in Fig.8(f) and Fig.8(g)). The dissymmetry is then amplified when increasing the shell volume (Fig.8(k)). As a result, the <111>fcc oriented grains also develop a dissymmetry of shape: the ones visible in Fig.8(j) have a larger extension than the ones visible in Fig.8(k) (their bases are respectively symbolized in blue and red in the pattern, Fig.8(c)).

(d) With all other patterns of any other group, the amplitude of the shell dissymmetry can amplify as described in (c) for the *4/m* group.

The 2D sections of the NP of group *4/m* are similar in the first step to the ones of group $m\bar{3}$ (Fig8(d) and Fig.8(g)) and $\bar{3}$ (Fig.8(e) and Fig.8(f)), but develop quite differently when the shell volume increases (Fig.8(h-k)). This illustrates that the lattice accommodation really needs to be considered in the three dimensions to build the shell and predict the dissymmetry.

F. Possible symmetries and morphologies of the experimental NP

The NP of Fig.3 can be symbolized by a partial pattern in Fig.10: the arrows represent the sequence of the four <111>fcc oriented variants to which we have access from the 2D section; the deduced elements of morphology are in yellow. It is not possible to fully reconstruct its morphology on the basis of the experimental image. Nevertheless, we can infer from Fig.10 that this NP possesses neither a center of symmetry, nor a 4, a $\overline{4}$ or a 2-fold axis, nor a mirror perpendicular to the observed 2D section. Its unique possible symmetry elements (in addition to the identity element) would be a mirror parallel to the 2D section or a 3-fold axis (from a <111>bcc axis). We infer that the only compatible groups are *3* (rhombohedral), *m* (monoclinic) and *1* (triclinic), all three being of low order of symmetry.

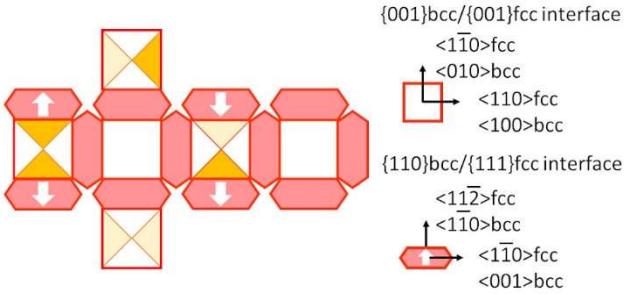

Fig.10 Partial pattern corresponding to the experimental image previously analyzed in Fig.3 (same variant sequence as displayed in 2D section in Fig.5(e)).

Fig.11 displays some possible patterns (a-c) with this selected experimental sequence and the corresponding 2D sections (d-i). In the first step of shell development, these 2D sections are similar, by construction (Fig.11(d-f)). Subtle differences develop later. With the 3-fold symmetry (Fig.11(g)), the left and top <001>fcc oriented grains have the same thickness, and so do the right and bottom grains. The larger dissymmetry of the experimental NP observed in 2D section, with the left pyramid significantly thicker than the three others visible <001>fcc oriented grains (Fig.3), is thus better supported by the hypothesis of group *m* or *1* (Fig.11(h-i)).

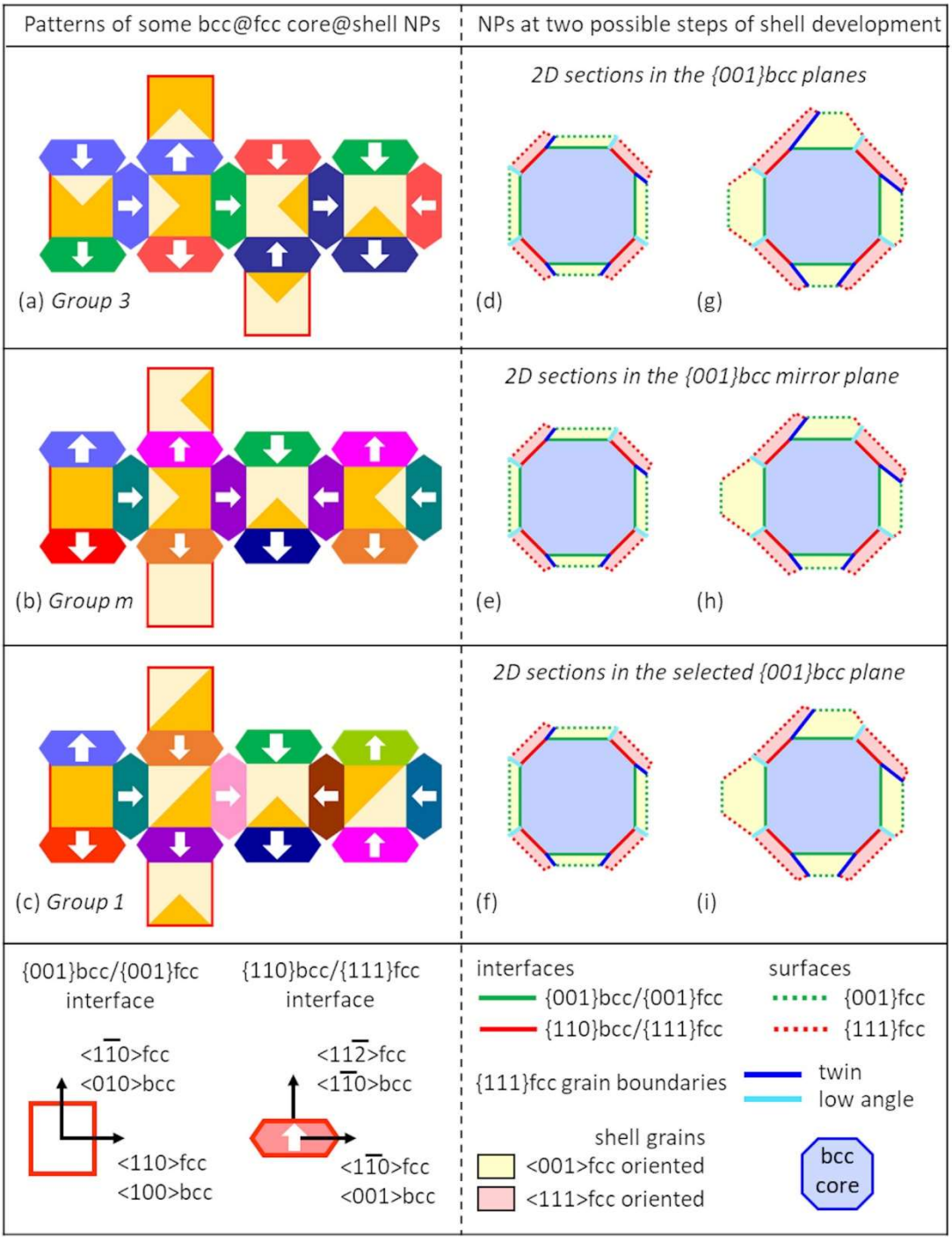

Fig.11 Patterns of some bcc@fcc core@shell NP morphologies with a symmetry compatible with the experimental sequence (Fig.3 and 10), respectively of group *3* (a), *m* (b) and *1* (c). The white arrows symbolize the variant distribution. The wider arrows reproduce the experimental sequence. The same color for the basis of the <111>fcc oriented grains means that they are symmetrical to each other. The light and dark yellow shades symbolize the morphology of the <001>fcc grains as defined in Fig.6(d). For each morphology, two steps of the shell development respecting the symmetry are proposed (d-i).

VI. Impact of the symmetry reduction of the core: cube-shaped core with and without truncations

The previous analysis can be extended to other core shapes with or without a high symmetry. This requires to decorrelate the effects of symmetry breakings due to the core shape or to the shell growth.

As an illustration, in this section we consider truncations on a cube-shaped core. This geometry is motivated by previous observations (Fig.12) of Fe@Au NPs with large irregular cores (typically in the range 10-20 nm) in contrast with NPs with well-formed cube-shaped small cores (typically in the range 5-10 nm) [30]. The large cores can be described as a mix between cubes and polyhedrons, with large {001}bcc/{001}fcc interfaces, smaller {110}bcc/{111}fcc interfaces and stepped interfaces, that are markers of the imperfect reorganization towards a cube-shaped core after coalescence of several smaller cores. (This is attributed to large energy barriers that have to be overcome for the interface to reach its equilibrium shape with such large cores). In addition, these NPs are off-centered with a dramatic dissymmetry in the Au pyramid size and shape [30].

In the following, symmetry breaking will be used relatively to the cube-shaped core symmetry.

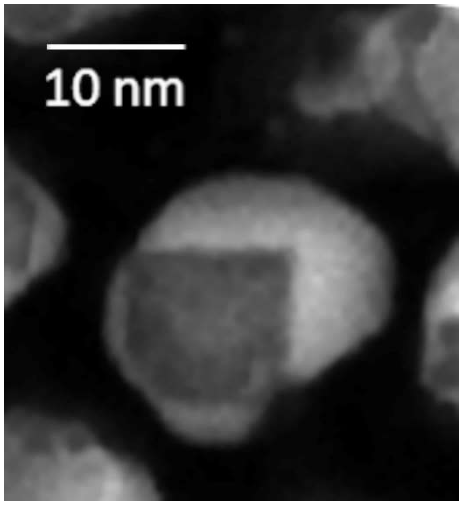

Fig.12 Low resolution HAADF-STEM image of a typical off-centered Fe@Au NP with a large Fe core.

A. NP symmetry with a cube-shaped core

Experimentally, cube-shaped Fe cores are generally well-centered and topped by six well-formed <001>fcc oriented Au pyramids growing on the {001}bcc faces [20, 26]. Note that there is no longer {111}fcc plane common to two adjacent grains, but a common <110>fcc direction. The grains are separated by grain boundaries approximately at 45° from their base (called 45° boundaries hereafter). These boundaries are coherent in the <110>fcc direction common to the two grains, but they are likely either to be incoherent in the perpendicular direction, or induce some elastic distortion, or both. Paradoxically, it is at the cost of a certain local disorder that the shell can adopt the same high symmetry as the core (cubic $m\bar{3}m$).

Fig.13 displays the patterns of the core (a) and of the NP morphology (b), both $m\bar{3}m$, and a 2D section where all pyramids are represented with the same aspect ratio (c). We chose the optimal aspect ratio that contributes to minimize the energy of the NPs, by balancing the {111}Au and {001}Au surfaces in this pyramidal configuration, from [20].

B. NP symmetry with a cube-shaped core truncated by {110}bcc faces

1. Single truncation

Fig.13(d) displays the case of a cube truncated by one {110}bcc face. For the core, the symmetry breaking compared to the cube lies in the additional face, but also in the different shapes and areas of the {001}bcc faces (respectively square, rectangular and pentagonal). This preserves two perpendicular mirrors, respectively one {001}bcc and one {110}bcc planes, and a 2-fold axis (the <110>bcc intersection of the mirrors). The core symmetry is thus *mm2.* (In this particular case, the Hermann-Mauguin notation needs to describe the iron in an orthorhombic lattice instead of the usual cubic one.)

The symmetry breaking due to the shell growth (Fig.13(e)) reduces the NP symmetry to the group *m*: only one mirror subsists once the variant of the {111}fcc oriented grain is determined (arrow). Note that a third type of boundary should exist between the <001>fcc oriented grains growing on pentagons and the <111>fcc oriented grain. There are now four different <001>fcc oriented grain morphologies. To symbolize them, four different colors are needed, depending on the nature of nearest boundary (Fig.13(e)): Light, medium or dark yellow when the neighbor grain is the

<111>fcc oriented grain with a twin boundary, a LAGB boundary or the third type of boundary respectively, and chestnut color when the neighbor will be another <001>fcc oriented grain separated by a 45° boundary. Three different <001>fcc oriented grain morphologies can be seen in 2D section in Fig.13(f).

(An adaptation of this model to describe the experimental case of non-cubic shells with cube-shaped cores is given in the Supplementary Material).

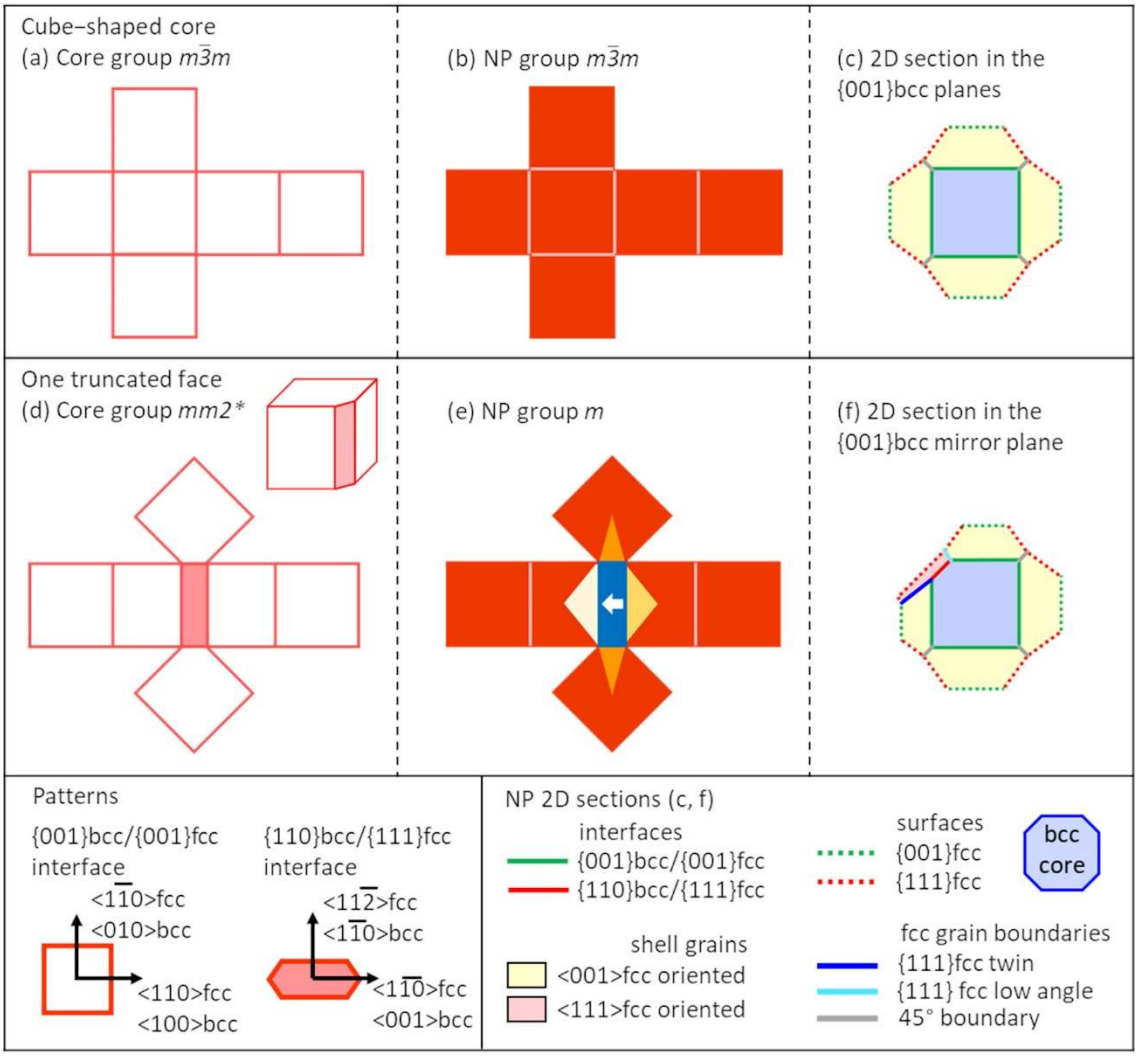

Fig.13 NP patterns with cube-shaped and truncated cube-shaped cores. The white arrow symbolizes the variant of the <111>fcc oriented grain growing on the {110}bcc truncated face. Light, medium or dark yellow shades indicate that the nearest neighbor of a <001>fcc oriented grain will be the <111>fcc oriented grain separated by a twin, a LAGB boundary or the third type of boundary, respectively, and chestnut color indicates that the neighbor will be another <001>fcc oriented grain separated by a 45° boundary. With a cube-shaped core (a), the NP (b) can remain in the group $m\bar{3}m$; (c) NP 2D section. With a single truncation, the core (d) and NP (e) belong to the *mm2* (*) and *m*

groups, respectively; (f) NP 2D section. (*) Here the Hermann-Mauguin notation needs to describe the core lattice in an orthorhombic lattice instead of the usual cubic one.

2. Generalization to any number of truncations (of same extension)

The symmetry reduction can be generalized as follows:

(i) First there is a symmetry breaking in the core directly due to the truncation, leading to a lower order than $m\bar{3}m$ and all other cubic groups. It results in a reduction of area and change in shape of the bases of the adjacent <001>fcc oriented grains, compared to others not affected by a truncation.

(ii) The NP symmetry is that of the variant distribution on the truncated faces.

(iii) If after truncation the core does no more possess {110}bcc mirror(s) and/or 2-fold axis perpendicular to a {110}bcc truncated face, the NP symmetry group can be identical to the core one, or is one of its sub-groups, depending on the variant distribution.

(iv) If the core still possesses one or some {110}bcc mirrors and/or 2-fold axis perpendicular to a {110}bcc truncated face, these elements are broken by the shell growth. Then the NP group is strictly a sub-group of the core group.

(An example of multiple truncation can be found in Supplementary Material.)

C. Consequences on the dissymmetrical development of the shell: experimental case of off-centered Fe@Au nanoparticles

Fig.14 displays an atomically resolved HAADF-STEM image of a Fe@Au NP with a large irregular core (adapted from [30]). The surfaces, interfaces, boundaries and grain orientations that are identifiable are indicated. There are three large {001}bcc/{001}fcc interfaces, two of them (at the bottom right) are separated by a small segment of {110}bcc/{111}fcc interface. It is then observed how a symmetry breaking is generated by the variant of the <111>fcc oriented grain and transmitted to the neighboring <001>fcc oriented grains by the LAGB and the twin boundary. On the top and right, thanks to the perfect cube-like shaped core, the two large <001>fcc oriented grains could have grown side by side, with a boundary more or less at 45° from their bases. Finally, the stepped interfaces top left and bottom left constitute other traces of the imperfect coalescence of several smaller cores, that also impacts the shell growth.

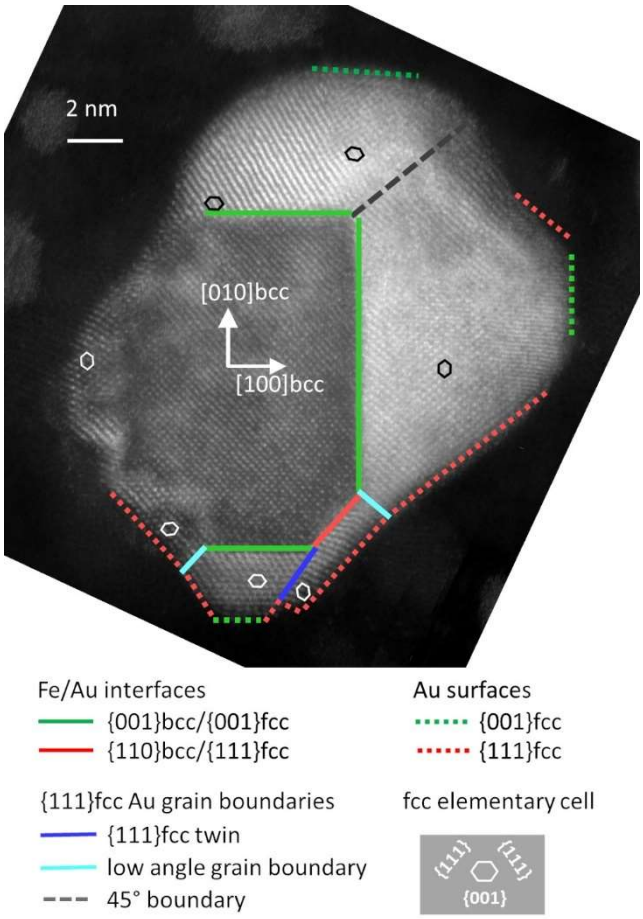

Fig.14 Atomically resolved HAADF-STEM image of an off-centered Fe@Au NP, observed along a <001>bcc direction.

The core pattern used in Fig.15 is a simplified model of this NP, where the irregularities of the interface are treated as three truncations from a perfect cube (the truncated faces being perpendicular to the observed 2D section). As we cannot presume of what happens in the third dimension, we do not consider other truncations. There are two possible configurations both of the *m* group.

Then we build the shell at different stages, with the same rules as in previous sections: the growth respects the symmetry, and similar grains have the same development. With the first configuration (Fig.15(a)), the two <001>fcc oriented grains on the left and bottom of the 2D section (Fig.15(b)) have a different morphology, while those on the top and right display the same morphology. This is reversed in the second configuration (Fig.15(c)): the grains on the left and bottom of the 2D section (Fig.15(d)) have the same morphology, while those on the top and right are different. In both configurations the left and bottom grains are limited in their development by their

boundaries, while the top ones are partially limited (Fig.15(d)) or not limited (Fig.15(b)) and the right ones are not.

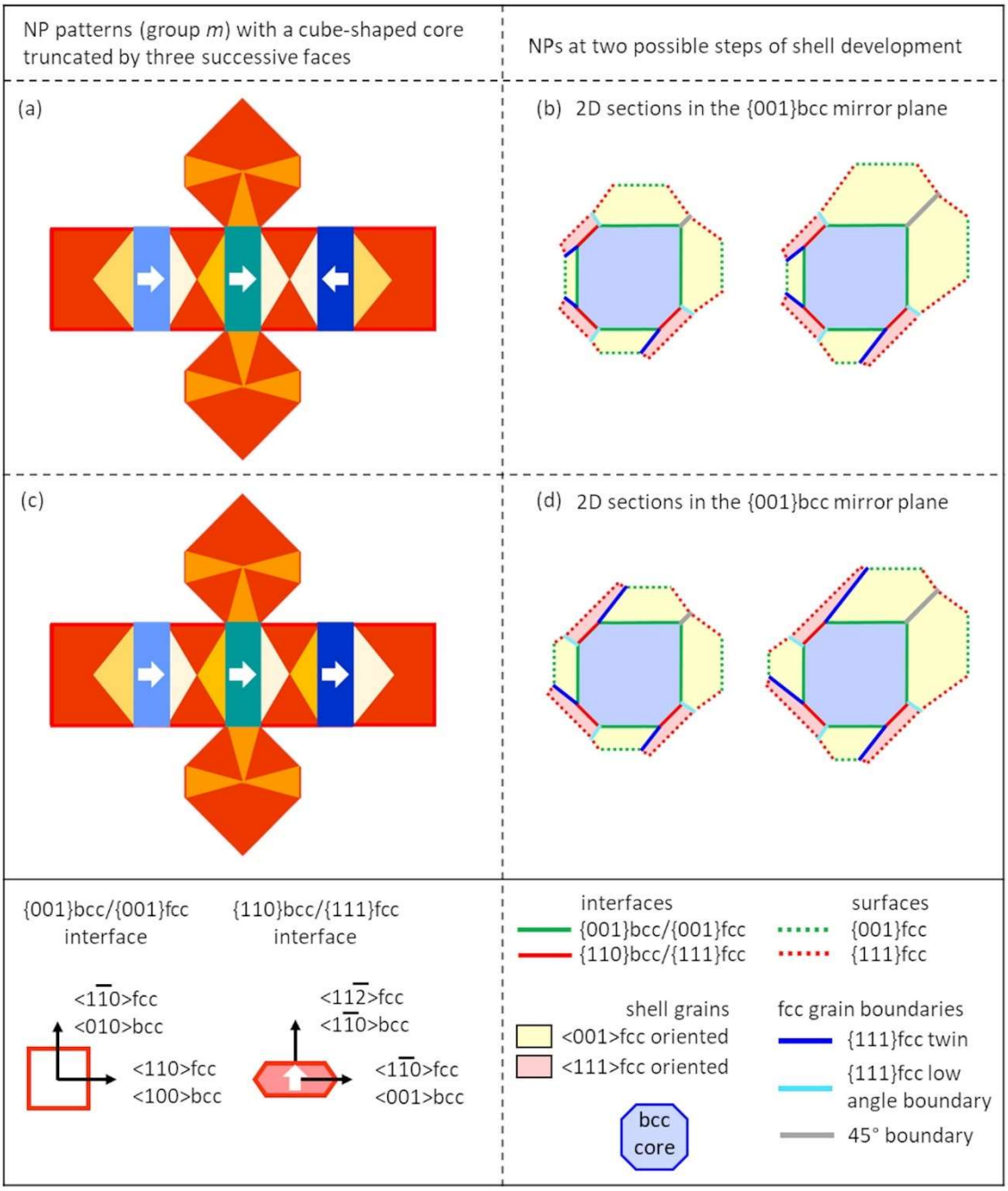

Fig.15 (a, c) Patterns of NPs with three truncations perpendicular to one {001}bcc plane. The white arrows symbolize the variants of <111>fcc oriented grains growing on the {110}bcc truncated faces. Light, medium or dark yellow shade indicate that the nearest neighbor of a <001>fcc oriented grain will be a <111>fcc oriented grain separated by a twin boundary, a LAGB boundary or the third type of boundary, respectively, and chestnut color indicates that the neighbor will be another <001>fcc grain separated by a 45° boundary. (b, d) 2D sections in the mirror plane at different possible stages of the shell evolution.

Another indirect consequence of the symmetry breaking can now be highlighted: with a cube-shaped core, thanks to the position of the 45° boundaries on symmetry planes, the pyramids can develop not only symmetrically, but also homothetically. As a result, the optimal shape of the pyramids that minimizes the NP energy by balancing the {111}fcc and {001}fcc facets [20] can be preserved (Fig.13(c)). Here however, the homothetic development of the surface is no longer possible (nor for any NPs with <111>fcc oriented grain(s)). The junction of the two large pyramids (Fig.15(b) and Fig.15(d)) is therefore probably the optimal solution for minimizing the surface energy: the shell is then more compact and preserves the balance between the two kinds of facets more than it would without the junction.

This mechanism dramatically amplifies the shell dissymmetry and leads to off-centered NPs as seen experimentally. The same mechanism was also at work in the NP of Fig.12.

D. Generalization of the respective roles of the core and the shell in the dissymmetrical shell development

The roles of core and shell can be decorrelated as follows:

(i) The symmetry reduction of the core shape impulses itself a dissymmetry in the shell, by generating different sizes and shapes for the grain bases. (A wide variety of {001}bcc faces can be created on a truncated cube-shaped core, including the ones seen in Fig.13(d) and Fig.15). In addition, the {110}bcc faces can in turn form ten possible different shapes (amongst them rectangle (Fig.13(d)), hexagon (Fig.6)).

(ii) Without further loss of symmetry due to the shell growth, there are as many different grain morphologies as different core face types (as in Fig.15).

(iii) A second symmetry loss, that occurs if the variant symmetry is lower than the core symmetry (which is most likely), increases the number of different grain types (for instance, 4 different <001>fcc oriented grain types in Fig.13(e) versus 3 different {001}bcc faces in Fig.13d). (Another example can be found in the Supplementary Material.)

(iv) In any case, the shell extension becomes more and more dissymmetrical as the shell volume increases, through the same mechanisms as in section V.E.

(v) A more indirect effect is due to the optimization of the surface (in terms of energy): it could be satisfied only at the cost of an even larger amplification of the shell dissymmetry, without further modification of the symmetry, as in Fig.15.

The dramatic dissymmetrical Au shell observed with large and irregular Fe cores is accounted for by these cumulated effects. The experimental NPs are not as perfect as in the models, but the same approach could be used with other deviations from the perfect cube-shaped core, as stepped interfaces or various core face sizes, and with other core shapes. In any case, even if by sake of simplicity the model considers only truncations, considering the lattice accommodation and its consequences succeeds in predicting off-centered NPs.

VII. Conclusion

Bcc@fcc multi-metallic NPs associate a monocrystalline core (Fe, FeCo…) with a polycrystalline shell (Au, AuAg…) consisting in 6 <001>fcc oriented grains growing on the {001}bcc faces of the core and up to 12 <111>fcc oriented grains growing on the {110}bcc faces of the core. They display various morphologies from perfect symmetrical ones to more irregular and strongly asymmetrical ones. In most cases they still present a high degree of crystalline organization, regardless their symmetry or asymmetry.

We here elucidated how these various morphologies are produced, by combining experimental analysis and theoretical analysis of their symmetry.

First the lattice accommodation was comprehensively analyzed, the core being assimilable to a nano-substrate and the shell to an epitaxially grown layer that has to adapt to each core face. Beyond the accommodation of the fcc shell lattice with the bcc core lattice through the two well-known Bain and Nishiyama-Wasserman epitaxial relationships (respectively coherent and semi-incoherent), here we also very clearly evidenced the lattice accommodation within the polycrystalline shell itself, that reveals a certain paradox. Two neighbor grains respectively <111>fcc and <001>fcc oriented are accommodated between them in a fully coherent manner either by a {111}fcc low angle grain boundary or a twin, but at the price of a strong internal stress (elastic distortion) due to geometrical constrains (existence of an angular gap).

It is then shown that the detailed morphology of such a bcc@fcc NP results from a chain of events where these different lattice accommodations play a central role. The core-shell interface tends in principle to its equilibrium shape, either a truncated rhombic dodecahedron or a cube, depending on the interface energies at play [20, 32], with eventual irregularities (truncations of the

cube, irregular face sizes…) due to kinetic limitations [30]. This however is not enough to determine the shell morphology: the arrangement of the <111>fcc and <001>fcc oriented grains really needs to be considered in the whole shell, in a 3D nano-puzzle-like organization driven by the lattice accommodation. As there are two possible variants of <111>fcc oriented grains (due to two possible directions of {111}fcc planes stacking on a {110}bcc face at the NW interfaces), the morphology of each <001>fcc oriented grain depends on the orientation of its four <111>fcc oriented neighbors.

Some elements of the core symmetry are likely to be broken. The symmetry of the whole NP is that of the shell, which cannot be higher than that of the core. It is thus reduced to the symmetry common to the core and to the distribution of the <111>fcc oriented grain variants. The symmetry analysis is here helpful to predict the possible morphologies within a frame common to any core shape:

(i) When the core is a rhombic dodecahedron truncated by {001}bcc faces (a 18 faces polyhedron), as experimentally observed for Fe@AuAg NPs (this work), there are (in theory) 186 different possible morphologies of NPs, distributed in 13 different symmetry groups. At the best the NP has a cubic symmetry $m\bar{3}$ of lower order than the core ($m\bar{3}m$) or a tetragonal symmetry *4/m*. However, it has more likely an even lower order of symmetry (sub-groups of $m\bar{3}$ and *4/m* groups). The probability for a NP to have a particular symmetry by pure chance is only 20%. Despite these symmetry breakings (or thanks to them…), and even in the case where the morphology is fully asymmetrical, the 6 <001>fcc oriented grains of the shell can be fully coherently accommodated with the 12 <111>fcc oriented grains, preserving a very good crystalline organization.

(ii) When the core is a {001}bcc cube, as experimentally observed in Fe@Au NPs with small cores [20, 22, 26] (or in FeCo@Au NPs [24]), the same cubic symmetry as the core ($m\bar{3}m$) can be achieved for the NP.

(iii) When the core is a {001}bcc cube truncated by {110}bcc faces, as experimentally observed in Fe@Au NPs with large cores [30], the NP symmetry is reduced to the symmetry common to the core and to the distribution of variants of the <111>fcc oriented grains growing on the truncated faces (this can be extended to other core shapes). The highly dissymmetrical development of the shell observed experimentally (off-centered NPs) is elucidated as being an indirect but spectacular consequence of the symmetry breakings induced by the truncations.

Characterizing the morphologies of polycrystalline NPs is challenging and often fragmentary, because of their size, the superposition of several grains and the fact that we have access to 2D sections only. The experimental NPs are not as perfect as in theory. In spite of this, reasoning by symmetry is a fruitful key to propose 3D models of morphologies that obey to a common and logical

growth scheme while reproducing satisfactorily the various observations. It allows to decorrelate the different effects that affect in chain the NPs, as the consequences of symmetry breakings originating from the core or from the shell, and their indirect consequences, leading for instance to the dramatic dissymmetry of off-centered NPs.

Reasoning by symmetry is also helpful in predicting the NP population homogeneity. This analysis indeed highlights an important characteristic of these bcc@fcc systems and similar polycrystalline nanostructures: not only a NPs population presents a size and eventually composition distribution, but it also could present a distribution of symmetry and a distribution of morphologies, even with a perfectly symmetric core.

Dissymmetry of NPs is not a priori detrimental to their properties, especially those that could be tuned by symmetry reduction, as in plasmonic applications [6, 8-10], or those driven by the nature and size of the exposed surfaces (for applications in catalysis, bio-functionalization…) [6, 11-13]. Exploiting the symmetry breaking or living with it requires to understand its origin and predict the variability of the population [4, 5]. Reliable distributions of morphologies are essential for the analyses of physical or chemical properties and for their prediction. The studied system is a case study illustrating the powerfulness of reasoning by symmetry for this objective.

SUPPLEMENTARY MATERIAL

I. Lattice accommodation and residual misfits at the bcc-fcc interfaces. II. Patterns of all possible bcc(core)@fcc(shell) NP morphologies with an 18 faces core (truncated rhombic dodecahedron), exhaustive for all symmetry groups except for groups *m* and *1*, and with mention of chiral character if applicable. III. Examples of dissymmetric NPs with a cube-shaped core and with a truncated cube-shaped core.

Acknowledgment

AP gratefully thanks A. Rossignol for his help with the numerical verification of Table I.

AUTHOR DECLARATIONS

Conflict of Interest

The authors have no conflicts to disclose.

Author Contributions

Anne Ponchet: Conceptualization (lead); Formal Analysis (lead); Visualization (lead); Writing/Original Draft Preparation (lead); Writing/Review & Editing (equal). **Nathalie Tarrat:** Conceptualization (equal); Formal Analysis (equal); Writing/Original Draft Preparation (supporting); Writing/Review & Editing (equal). **Teresa Hungria:** Investigation (equal); Writing/Review & Editing (equal). **Magali Benoit:** Conceptualization (equal); Writing/Original Draft Preparation (supporting); Writing/Review & Editing (equal). **Marie-José Casanove:** Conceptualization (equal); Investigation (equal); Writing/Original Draft Preparation (supporting); Writing/Review & Editing (equal). **Patrizio Benzo:** Conceptualization (equal); Investigation (lead); Writing/Original Draft Preparation (supporting); Writing/Review & Editing (equal).

DATA AVAILABILITY

The data that support the findings of this study are available from the corresponding author upon reasonable request.

APPENDIX A: Disorientation between the fcc grains in the shell, with a truncated rhombic dodecahedron bcc core

Fig.16 shows schematically the virtual arrangements of grains in relaxed state (represented with a thickness significantly larger than the experimental shell thickness). Only one quadrant consisting in one grain with the <111>fcc orientation (Grain 2) and two half grains with the <001>fcc orientation (Grain 1 and Grain 3) is shown.

I. Angular gap per quadrant

Grain 2 requires an angle of 109.47° between its two families of {111}fcc planes, one of them being parallel to the interface (in red). The angular aperture between the corresponding {111}fcc planes in

Grain 1 and Grain 3 is given by their disorientation $\theta_{1/3} = 90°$. The angular gap per quadrant is thus: 90° - 109.47° = -19.47°.

II. Disorientation and angular gap at each boundary

As the angle between {001}fcc and {111}fcc planes is 54.74°, the disorientation $\theta_{1/2}$ between Grain 1 and Grain 2 is: $\theta_{1/2} = 54.74° + 45° - 109.47° = -9.74°$. The disorientation between Grain 2 and Grain 3 is: $\theta_{2/3} = \theta_{1/3} - \theta_{1/2} = 99.74°$. Given that the disorientation accommodated by a twin is $\theta_{twin} = 2x54.74°$, the residual disorientation is: $\theta_{res2/3} = \theta_{2/3} - \theta_{twin} = -9.74°$. The angular gaps per boundary are $\theta_{1/2}$ and $\theta_{res2/3}$ at the LAGB and twin boundary, respectively.

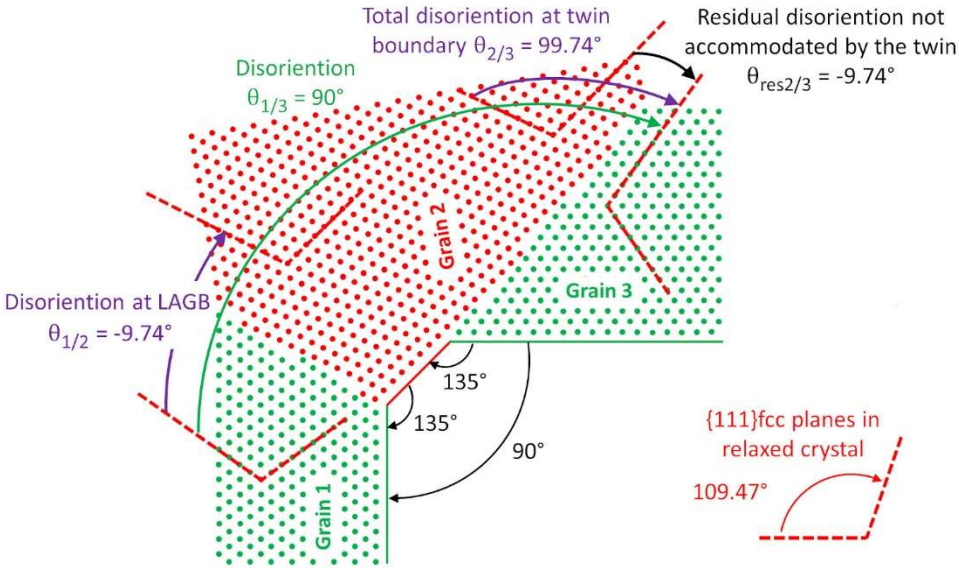

Fig. 16. Scheme of fcc grain arrangement in the shell, in relaxed state, represented with a larger thickness than the experimental shell thickness. The green and red grains are <001>fcc and <111>fcc oriented respectively, and are plastically accommodated by a LAGB (left boundary) and a twin (right boundary).

III. Distance between dislocations along the boundaries, with the grains in relaxed state

Fig.16 shows graphically that one dislocation approximatively every six atomic planes along each boundary is required to plastically accommodate the grains between them. (The distance D between two dislocations along a LAGB can also be calculated as $D \approx b/\theta_{1/2}$, where b is the modulus of the edge component of their Burgers vector. It comes that the number of {111}fcc atomic planes separating two dislocations is $1/\theta_{1/2} \approx 5.9$.)

APPENDIX B: Calculation of symmetry and morphology distribution of bcc@fcc nanoparticles with a truncated rhombic dodecahedron core

I. Calculation of n(*G*)

Each of the 12 {110}bcc faces generates two possibilities for the variants of <111>fcc oriented grains so that there are 2^{12} possible combinations. To calculate n(G), the number of combinations for each particular symmetry group *G*, the degrees of freedom are reduced by symmetry as follows:

Super-group $m\bar{3}$: Once one of the twelve variants is determined, there is no more degree of freedom, thus $\mathrm{n}(m\bar{3}) = 2^1$.

Super-group *4/m*: The 4-fold axis (built from a <001>bcc direction) reduces the degrees of freedom from 12 to 3. The mirror perpendicular to the 4-fold axis reduces them to 2. As there are 3 different possible 4-fold axes, it comes $\mathrm{n}(4/m) = 3 \times 2^2$.

Sub-groups: the principle is similar. However, it is necessary to remove all combinations already counted in the super-groups of *G* (from Fig.7). Example for *2/m*: The 2-fold axis (built from a <001>bcc direction) reduces the degrees of freedom from 12 to 6. The mirror perpendicular to the 2-fold axis reduces them to 4. Considering the 3 different possible 2-fold axis and removing the combinations already counted in the super-groups of *2/m* (Fig.7), it comes $\mathrm{n}(2/m) = 3\left(2^4 - \mathrm{n}(mmm) - \mathrm{n}(m\bar{3})\right) - \mathrm{n}(4/m)$.

II. Calculation of q(*G*)

From one initial pattern, there are 4x3x2 =24 possible permutations giving a similar variant distribution (4 by rotation of $2\pi/4$ around one <001>bcc axis, 3 by rotation of $2\pi/3$ around one <111>bcc axis, 2 by rotation of π around another <001>bcc axis). The patterns obtained by permutation that are directly superposable to the initial pattern without translation or rotation are due to the same combination amongst the 2^{12} ones. The number of different combinations giving the same variant distribution, q(*G*), is thus equal to the number of permutations that provide a pattern not directly superposable to others without translation or rotation (some examples in Fig.17). It can be deduced from symmetry as follows: (i) If at least one <111>bcc axis is a 3-fold axis, the number of combinations is reduced by 3 from 24. (ii) If one <001>bcc axis is a 4-fold axis, the

number of combinations is reduced by 4. (iii) If at least one <001>bcc axis is a 2-fold axis but not a 4-fold axis, the number of combinations is reduced by 2. (iv) If there is another 2-fold axis, the number of combinations is reduced by 2. It comes:

q($m\bar{3}$) = 24/(3x2x2) = 2 ; q(*3*) = q($\bar{3}$) = 24/3 = 8 ; q(*4/m*) = q(*4*) = 24/4 = 6 ; q(*mmm*) = 24/(2x2) = 6 ; q($\bar{4}$) = q(*mm2*) = q(*2/m*) = q(*2*) = 24/2 = 12 ; q(*m*) = q($\bar{1}$) = q(*1*) = 24

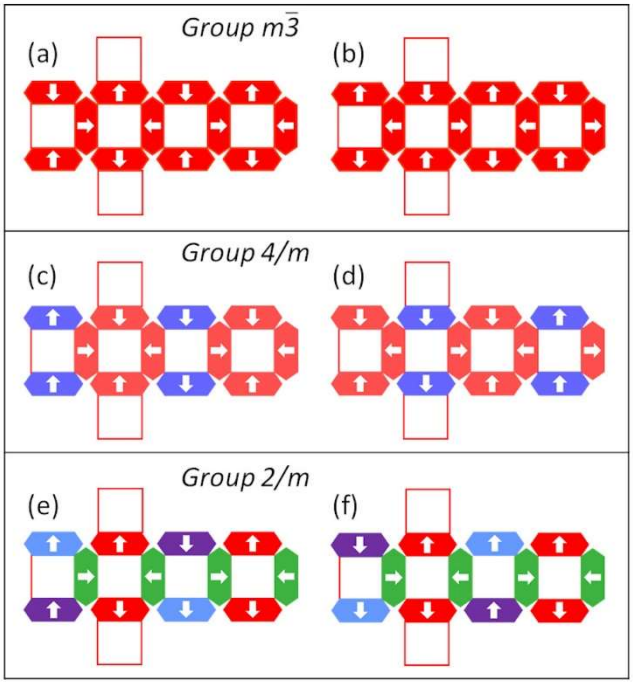

Fig.17. Group $m\bar{3}$ (a-b): the initial pattern (a) and its permutation by a $2\pi/4$ rotation (b) are similar but not directly superposable without translation or rotation. Patterns obtained by all other permutations are directly superposable to either (a) or (b). There are only two different combinations. Group *4/m* (c-d): the patterns obtained by permutation by $2\pi/4$ rotation around the 4-fold axis are directly superposable to the initial one (c); as example, a pattern obtained by permutation by $2\pi/3$ rotation around a <111>bcc axis (d) is not. There are 6 different combinations. Group *2/m* (e-f): the pattern obtained by permutation by a π rotation around the 2-fold axis is directly superposable to the initial one (e); as example, a pattern obtained by permutations by $\pi/2$ rotation around another <001>bcc axis is not. There are 12 different combinations.

III. Calculation of p(*G*)

The number of different morphologies p(*G*) is deduced from n(*G*) = p(*G*) x q(*G*).

REFERENCES

[1] R. Ferrando, J. Jellinek, Roy L. Johnston, Chem. Rev., 108, 845 (2008)

[2] D. Ferrer, A. Torres-Castro, X. Gao, S. Sepulveda-Guzman, U. Ortiz-Mendez and M. Jose-Yacaman, Nano Letters, 7, 1701 (2007)

[3] L. Piccolo, Z.Y. Li, I. Demiroglu, F. Moyon, Z. Konuspayeva, G. Berhault, P. Afanasiev, W. Lefebvre, Jun Yuan and Roy L. Johnston, Scientific Reports, 6, 35226 (2016)

[4] L D Marks and L Peng, J. Phys.: Condens. Matter, Vol. 28, p. 053001 (2016)

[5] Kyle D. Gilroy, Hsin-Chieh Peng, Xuan Yang, Aleksey Ruditskiy and Younan Xia, Chem. Commun., 53, 4530 (2017)

[6] Zachary J. Woessner and Sara E. Skrabalak, J. Phys. Chem. C, 125, 23587 (2021)

[7] Gyeong-Su Park, Kyung Suk Min, Hyuksang Kwon, Sangwoon Yoon, Sangwon Park, Ji-Hwan Kwon, Sangmin Lee, Jaeyeon Jo, Miyoung Kim, and Seong Keun Kim, Adv. Mater., 33, 2100653 (2021)

[8] Roy L. Johnston and Andrew J. Logsdail, J. Phys. Chem. C, V116, 23616 (2012)

[9] Elyahb Allie Kwizera, Elise Chaffin, Xiao Shen, Jingyi Chen, Qiang Zou, Zhiming Wu, Zheng Gai, Saheel Bhana, Ryan O'Connor, Lijia Wang, Hitesh Adhikari, Sanjay R. Mishra, Yongmei Wang, and Xiaohua Huang, J. Phys. Chem. C, 120, 10530 (2016)

[10] Asep Sugih Nugraha, Olga Guselnikova, Joel Henzie, Jongbeom Na, Md Shahriar A. Hossain, Ömer Dag, Alan E. Rowan, and Yusuke Yamauchi, Chem. Mater., 34, 7256 (2022)

[11] Q. Zhang and H. Wang, ACS Catal., 4, 4027 (2014)

[12] P. Chen, K. Murugappan and Martin R. Castell, Phys. Chem. Chem. Phys., 22, 4416 [2020]

[13] Muhammad Iqbal, Yoshio Bando, Ziqi Sun, Kevin C.-W. Wu, Alan E. Rowan, Jongbeom Na, Bu Yuan Guan and Yusuke Yamauchi, Adv. Mater., 33, 2004554 (2021)

[14] Riccardo Ferrando, J. Phys.: Condens. Matter, 27, 013003 (2015)

[15] D. Bochicchio and R. Ferrando, Physical Review B, Vol. 87, p. 165435 (2013)

[16] C. Langlois, Z.L. Li, Jun Yuan, D. Alloyeau, J. Nelayah, D. Bochicchio, R. Ferrando and C. Ricolleau, Nanoscale, 4, 3381 (2012)

[17] E. Bauer and Jan H. van der Merwe, Phys. Rev. B, 33, 3657 (1986)

[18] H. F. Jurca, A. Damian, C. Gougaud, D. Thiaudière, R. Cortès, F. Maroun and P. Allongue, J. Phys. Chem. C, 120, 16080 (2016)

[19] W.R. Miller and W.A. Tyson, Surface Science 62, 267 (1977)

[20] A. Ponchet, S. Combettes, P. Benzo, N. Tarrat, M. J. Casanove, and M. Benoit, J. Appl. Phys., 128, 055307 (2020)

[21] H. Okamoto, T. Massalski, L. Swartzendruber, and P. Beck, Bulletin of Alloy Phase Diagrams 5, 592 (1984)

[22] C. Langlois, P. Benzo, R. Arenal, M. Benoit, J. Nicolai, N. Combe, A. Ponchet, and M. J. Casanove. Nano Letters 15, 5075 (2015).

[23] D. Amram and E. Rabkin, ACS Nano, 8, 10687 (2014)

[24] Yun-Hao Xu and Jian-Ping Wang, Appl. Phys. Lett., 91, 233107 (2007)

[25] P. Benzo, S. Combettes, C. Garcia, T. Hungria, B. Pécassou and M.J. Casanove. 2020, Cryst. Growth Des., 20, 4144 (2020)

[26] P. Benzo, S. Combettes, B. Pecassou, N. Combe, M. Benoit, M. Respaud, and M. J. Casanove, Phys. Rev. Mat., 3, 096001 (2019)

[27] L. Vitos, A. Ruban, H. Skriver, J. Kollár, Surface Science, 411, 186 (1998)

[28] Y. Saito, J. Cryst. Growth, 53, 273 (1981)

[29] S. Giorgio, C.R. Henry, C. Chapon, G. Nihoul, and J.M. Penisson, Ultramicroscopy, 38, 1 (1991)

[30] S. Combettes, T. Hungria, S. Barre, B. Pecassou, R. Cours, M. Benoit, M.-J. Casanove, A. Ponchet, and P. Benzo, Eur. Phys. J. Appl. Phys., 97, 27 (2022)

[31] Jin Li, Y. Chen, S. Xue, H. Wang, X. Zhang, Acta Materialia, 114, 154 (2016)

[32] S. Combettes, J. Lam, P. Benzo, A. Ponchet, M.-J. Casanove, F. Calvo, and M. Benoit, Nanoscale, 12, 18079 (2020)

[33] L. Golstein, F. Glass, J.Y. Marzin, M.N. Charasse and G. Leroux, Appl. Phys. Lett., 47, 1099 (1995)

[34] C.W. Snyder, B.G. Orr, D. Kessler and L.M. Sander, Phys. Rev. Lett., 66, 3032 (1991)

[35] D.J. Eaglesham and M. Cerullo, Phys. Rev. Lett., 64, 1943 (1990)

[36] S. Guha, A. Madhukar and K.C. Raykumar, Appl. Phys. Lett., 57, 2110 (1990)

[37] R. Kern and P. Müller, Surf. Sci., 392, 103 (1997)

[38] C. Priester and M. Lannoo, Phys. Rev. Lett., 75, 93 (1995)

[39] A. Ponchet, L. Pedesseau, A. Le Corre, C. Cornet and N. Bertru, Appl. Phys. Lett., 114, 173102 (2019)

[40] J. Tersoff and F.K. LeGoues, Phys. Rev. Lett., 72, 3570 (1994)

[41] A. Ponchet, D. Lacombe, L. Durand, D. Alquier, and J.-M. Cardonna, Appl. Phys. Lett., 72, 2984 (1998)

[42] Hahn, Theo, [ed.]. International tables for crystallography. Fifth edition: Published for the International Union of Crystallography by Springer pp. 795-796 (2005). Volume A: Space-Group Symmetry. ISBN 0-7923-6590-9.